Atmospheric energy budget response to idealized aerosol perturbation in tropical cloud systems

Guy Dagan[1], Philip Stier[1], Matthew Christensen[1], Guido Cioni[2,3], Daniel Klocke[3,4] and Axel Seifert[4]

[1] Atmospheric, Oceanic and Planetary Physics, Department of Physics, University of Oxford, UK

[2] Max Planck Institute for Meteorology, Hamburg, Germany

[3] Hans Ertel Center for Weather Research, Offenbach am Main, Germany

[4] Deutscher Wetterdienst, Offenbach am Main, Germany

E-mail: guy.dagan@physics.ox.ac.uk

Abstract

The atmospheric energy budget is analysed in numerical simulations of tropical cloud systems to better understand the physical processes behind aerosol effects on the atmospheric energy budget. The simulations include both shallow convective clouds and deep convective tropical clouds over the Atlantic Ocean. Two different sets of simulations, at different dates (10-12/8/2016 and 16-18/8/2016), are simulated with different dominant cloud modes (shallow or deep). For each case, the cloud droplet number concentrations (CDNC) is varied as a proxy for changes in aerosol concentrations without considering the temporal evolution of the aerosol concentration (for example due to wet scavenging which may be more important under deep convective conditions). It is shown that the total column atmospheric radiative cooling is substantially reduced with CDNC in the deep-cloud dominated case (by ~10.0 W/m^2), while a much smaller reduction (~1.6 W/m^2) is shown in the shallow-cloud dominated case. This trend is caused by an increase in the ice and water vapor content at the upper troposphere that leads to a reduced outgoing longwave radiation, an effect which is stronger under deep-cloud dominated conditions. A decrease in sensible heat flux (driven by increase in the near surface air temperature) reduces the warming by ~1.4 W/m^2 in both cases. It is also shown that the cloud fraction response behaves in opposite ways to an increase in CDNC, showing an increase in the deep-cloud dominated case and a decrease in the shallow-cloud dominated case. This demonstrates that under different environmental conditions the response to aerosol perturbation could be different.

Introduction

The negative anthropogenic radiative forcing due to aerosols is acting to cool the climate and to compensate some of the warming due to increase in greenhouse gases (Boucher et al., 2013). However, quantification of this effect is highly uncertain with a revised uncertainty range of -1.60 to -0.65 W/m^2 (Bellouin et al., 2019). The total anthropogenic aerosol radiative forcing is composed of contribution from direct interaction of aerosols with radiation (scattering and absorption) and from indirect interaction with radiation due to changes in cloud properties.

Beside its effect on the radiation budget, aerosols may affect the precipitation distribution and total amount (Levin and Cotton, 2009; Albrecht, 1989; Tao et al., 2012). A useful perspective to improve our understanding of aerosol effect on precipitation, which became common in the last few years, arises from constraints on the energy budget (O'Gorman et al., 2012; Muller and O'Gorman, 2011; Hodnebrog et al., 2016; Samset et al., 2016; Myhre et al., 2017; Liu et al., 2018; Richardson et al., 2018; Dagan et al., 2019a). On long time scales, any precipitation perturbations by aerosol effects will have to be balanced by changes in radiation fluxes, sensible heat flux or by divergence of dry static energy. The energy budget constraint perspective was found useful to explain both global (e.g. (Richardson et al., 2018)) and regional (Liu et al., 2018; Dagan et al., 2019a) precipitation response to aerosol perturbations in global scale simulations. In this study, we investigate the energy budget response to aerosol perturbation on a regional scale using high resolution cloud resolving simulations. This enables an improved understanding of the microphysical processes controlling atmospheric energy budget perturbations. The strong connection between the atmospheric energy budget and convection has long been appreciated (e.g. (Arakawa and Schubert, 1974; Manabe and Strickler, 1964)) as well as the connection to the general circulation of the atmosphere (Emanuel et al., 1994).

The total column atmospheric energy budget can be described as follows:

$$LP + Q_R + Q_{SH} = \mathrm{div}(s) + \mathrm{d}s/\mathrm{d}t \qquad (1)$$

Equation 1 presents a balance between the latent heating rate (LP - latent heat of condensation [L] times the surface precipitation rate [P]), the surface sensible heat flux (Q_{SH}), the atmospheric radiative heating (Q_R), the divergence of dry static energy (div(s), which will become negligible on sufficiently large spatial scales), and the dry static energy storage term (ds/dt, which will

become negligible on long [inter-annual] temporal scales). Throughout the rest of this paper we will refer to the right-hand side of Equation 1 (div(s)+ds/dt) as the energy imbalance (which is calculated as the residual [R] of the left-hand side).

Q_R is defined as:

$$Q_R = (\boldsymbol{F}_{SW}^{TOA} - \boldsymbol{F}_{SW}^{SFC}) + (\boldsymbol{F}_{LW}^{TOA} - \boldsymbol{F}_{LW}^{SFC}) \qquad (2)$$

and represents the rate of net atmospheric diabatic warming due to radiative shortwave (SW) and longwave (LW) fluxes. It is expressed by the sum of the surface (SFC) and top of the atmosphere (TOA) fluxes, when all fluxes are positive downwards. As in the case of TOA radiative forcing, aerosols could modify the atmospheric energy budget by both direct interaction with radiation and by microphysical effects on clouds. The latter is the focus of this study.

The microphysical effects are driven by the fact that aerosols serve as cloud condensation nuclei (CCN) and ice nuclei (IN). Larger aerosol concentrations, e.g. by anthropogenic emissions, could lead to larger cloud droplet and ice particle concentrations (Andreae et al., 2004; Twomey, 1977; Hoose and Möhler, 2012). Changes in hydrometer concentration and size distribution were shown to affect clouds' microphysical processes rates (such as condensation, evaporation, freezing and collision-coalescence), which in turn could affect the dynamics of the clouds (Khain et al., 2005; Koren et al., 2005; Heikenfeld et al., 2019; Chen et al., 2017;Altaratz et al., 2014; Seifert and Beheng, 2006a), the rain production (Levin and Cotton, 2009; Albrecht, 1989; Tao et al., 2012) and the clouds' radiative effect (Koren et al., 2010; Storelvmo et al., 2011; Twomey, 1977; Albrecht, 1989). The aerosol effect, and in particular its effects on the radiation budget and the atmospheric energy budget, is cloud regime dependent (Altaratz et al., 2014; Lee et al., 2009; Mülmenstädt and Feingold, 2018; van den Heever et al., 2011; Rosenfeld et al., 2013; Glassmeier and Lohmann, 2016; Gryspeerdt and Stier, 2012; Christensen et al., 2016), time dependent (Dagan et al., 2017; Gryspeerdt et al., 2015; Seifert et al., 2015; Lee et al., 2012; Dagan et al., 2018c), aerosol type and size distribution dependent (Jiang et al., 2018; Lohmann and Hoose, 2009) and (even for a given cloud regime) meteorological conditions dependent (Dagan et al., 2015a; Fan et al., 2009; Fan et al., 2007; Kalina et al., 2014; Khain et al., 2008) and was shown to be non-monotonic (Dagan et al., 2015b; Jeon et al., 2018; Gryspeerdt et al., 2019; Liu et al., 2019). Hence the quantification of the global mean radiative effect is extremely challenging (e.g. (Stevens and Feingold, 2009; Bellouin et al., 2019)).

Previous studies demonstrated that the mean aerosol effect on deep convective clouds can increase the upward motion of water, and hence also increase the cloud anvil mass and extent (Fan et al., 2010; Chen et al., 2017; Fan et al., 2013; Grabowski and Morrison, 2016). The increase in mass flux to upper levels was explained by the convective invigoration hypothesis (Fan et al., 2013; Koren et al., 2005; Rosenfeld et al., 2008; Seifert and Beheng, 2006a; Yuan et al., 2011a; Williams et al., 2002), which was proposed to lead to stronger latent heat release under higher aerosol concentrations and hence stronger vertical velocities. In addition to the stronger vertical velocities, under polluted conditions the smaller hydrometers are being transported higher in the atmosphere (for a given vertical velocity (Chen et al., 2017; Koren et al., 2015; Dagan et al., 2018a)) and their lifetime at the upper troposphere is longer (Fan et al., 2013; Grabowski and Morrison, 2016). The invigoration mechanism can also lead to an increase in precipitation (Khain, 2009; Altaratz et al., 2014). Both the increase in precipitation and the increase in anvil coverage would act to warm the atmospheric column: the increased precipitation by latent heat release, and the increased anvil mass and extent by longwave radiative warming (Koren et al., 2010; Storelvmo et al., 2011). However, it should be pointed out that the uncertainty underlying these proposed effects remain significant (White et al., 2017; Varble, 2018). In addition, aerosol effects on precipitation from deep convective cloud was shown to be non-monotonic and depend on the aerosol range (Liu et al., 2019).

In the case of shallow clouds, aerosol effect on precipitation was also shown to be non-monotonic (Dagan et al., 2015a; Dagan et al., 2017). However, unlike in the deep clouds case, the mean effect on precipitation, under typical modern-day conditions, is thought to be negative (Albrecht, 1989; Rosenfeld, 2000; Jiang et al., 2006; Xue and Feingold, 2006; Dagan and Chemke, 2016). The aerosol effect on shallow cloud cover and mean water mass (measure by liquid water path - LWP) might also depend on the meteorological conditions and aerosol range (Dagan et al., 2015b; Dagan et al., 2017; Gryspeerdt et al., 2019; Dey et al., 2011; Savane et al., 2015) and is the outcome of competition between different opposing response of: rain suppression (that could lead to increase in cloud lifetime and coverage (Albrecht, 1989)), warm clouds invigoration (that could also lead to increase in cloud coverage and LWP (Koren et al., 2014; Kaufman et al., 2005; Yuan et al., 2011b)) and increase in entrainment and evaporation (that could lead to decrease in cloud coverage (Small et al., 2009; Jiang et al., 2006; Costantino and Bréon, 2013; Seigel, 2014)). Another addition to this complex response is the fact that the aerosol effect on warm convective clouds was shown to be time dependent and affected by the clouds' feedbacks on the thermodynamic conditions (Seifert et al., 2015; Dagan et al., 2016; Dagan et al., 2017; Lee et al.,

2012; Stevens and Feingold, 2009; Dagan et al., 2018b). Previous simulations that contained several tropical cloud modes demonstrate that increase in aerosol concentrations can lead to suppression of the shallow mode and invigoration of the deep mode (van den Heever et al., 2011). Hence the domain mean effect, even if it is demonstrated to be small, may be the result of opposing relatively large contributions from the different cloud modes (van den Heever et al., 2011). The small domain mean effect may suggest that on large enough scales the energy (Muller and O'Gorman, 2011; Myhre et al., 2017) or water budget (Dagan et al., 2019b) constrain precipitation changes.

Previous studies, using global simulations (O'Gorman et al., 2012; Muller and O'Gorman, 2011; Hodnebrog et al., 2016; Samset et al., 2016; Myhre et al., 2017; Liu et al., 2018; Richardson et al., 2018; Dagan et al., 2019a), demonstrated the usefulness of the atmospheric energy budget perspective in constraining aerosol effect on precipitation. However, the physical processes behind aerosol-cloud microphysical effects on the energy budget are still far from being fully understood. In this study we use cloud resolving simulations to increase our understanding of the effect of microphysical aerosol-cloud interactions on the atmospheric energy budget.

Methodology

The icosahedral nonhydrostatic (ICON) atmospheric model (Zängl et al., 2015) is used in a limited area configuration. ICON's non-hydrostatic dynamical core was evaluated with several idealized cases (Zängl et al., 2015). The simulations are conducted such that they are aligned with the NARVAL 2 (Next-generation Aircraft Remote-Sensing for Validation Studies (Klepp et al., 2014; Stevens et al., 2019; Stevens et al., 2016)) campaign, which took place during August 2016 in the western part of the northern tropical Atlantic. We use existing NARVAL 2 convection-permitting simulations (Klocke et al., 2017) as initial and boundary conditions for our simulations.

The domain covers ~22^{o} in the zonal direction (25^{o} - 47^{o} W) and ~11^{o} in the meridional direction (6^{o} - 17^{o} N) and therefore a large fraction of the northern tropical Atlantic (Fig. 1). During August 2016, the intertropical convergence zone (ITCZ) was located in the southern part of the domain while the northern part mostly contains trade cumulus clouds. Hence, this case study provides an opportunity to study heterogenous clouds systems. Daily variations in the deep/shallow cloud modes in our domain were observed, but it always included both cloud modes, albeit in different relative fraction. Two different dates are chosen, one representing a shallow-cloud dominated

mode (10-12/8/2016 – see Fig. 2, and Figs S1 and S3, supporting information- SI), and one that represents a deep-cloud dominated mode (16-18/8/16 – see Fig. 3 and Figs. S2 and S3, SI). In the shallow-cloud dominated case, most of the domain is covered by trade cumulus clouds that are being advected with the trade winds from north-east to south-west. In the southern part of the domain, throughout most of the simulation, there is a zonal band of deep convective clouds (Fig. 2) that contribute on average ~25% out of the total cloud cover (Fig. S3, SI). The deep-cloud dominated case represents the early stages of the development of the tropical storm Fiona (Fig. 3). Fiona formed in the eastern tropical Atlantic and moved toward the west-north-west. It started as a tropical depression at 16/8/2016 18:00 UTC while its centre was located at 12.0º N 32.2º W. It kept moving towards the north-west and reach a level of a tropical storm at 17/8/2016 12UTC, while its centre was located at 13.7º N 36.0º W (https://www.nhc.noaa.gov/data/tcr/AL062016_Fiona.pdf). The general propagation speed and direction, strength (measure by maximal surface wind speed) and location of the storm are predicted well by the model. However, the model produces more anvil clouds than what was observed from the satellite (Fig. 3). These two different cases, representing different atmospheric energy budget initial state (see also Figs. 4 and 12 below), enable the investigation of the aerosol effect on the energy budget under different initial conditions.

We use a two-moment bulk microphysical scheme (Seifert and Beheng, 2006b). For each case, four different simulations with different prescribed cloud droplet number concentrations (CDNC) of 20, 100, 200, and 500 cm^{-3} are conducted. The different CDNC scenarios serve as a proxy for different aerosol conditions (as the first order effect of increased aerosol concentration on clouds is to increase the CDNC, Andreae, 2009). This also allows to separate the cloud response from the uncertainties involved in the representation of the aerosols in numerical models (Ghan et al., 2011; Simpson et al., 2014; Rothenberg et al., 2018). However, it limits potential feedbacks between clouds and aerosols, such as the removal of aerosol levels by precipitation scavenging and potential aerosol effects thereon. In addition, the fixed CDNC framework does not capture the differences in aerosol activation between shallow and deep clouds, due to differences in vertical velocity. Another aerosol effect that is not included in our simulations is the direct interaction between aerosol and radiation. In future work we plan to examine the mutual interaction between the microphysical effects and the direct aerosol radiative effects.

For calculation of the difference between high CDNC (polluted) conditions and low CDNC (clean) conditions, the simulations with CDNC of 200 and 20 cm^{-3} are chosen as they represent the range typically observed over the ocean (see for example the CDNC range presented in recent observational-based studies (Rosenfeld et al., 2019; Gryspeerdt et al., 2019)). Each simulation is conducted for 48 hours starting from 12 UTC. The horizontal resolution is set to 1200 m and 75 vertical levels are used. The temporal resolution is 12 sec and the output interval is 30 min. Interactive radiation is calculated every 12 min using the RRTM-G scheme (Clough et al., 2005; Iacono et al., 2008; Mlawer et al., 1997). We have added a coupling between the microphysics and the radiation to include the Twomey effect (Twomey, 1977). This was done by including the information of the cloud liquid droplet effective radius, calculated in the microphysical scheme, in the radiation calculations. No Twomey effect due to changes in the ice particles size distribution was considered due to the large uncertainty involved in the ice microphysics and morphology. Additional details, such as the surface and atmospheric physics parameterizations, are described in Klocke et al., (2017) and include an interactive surface flux scheme and fixed sea surface temperature (SST). We note that using a fixed SST does not include feedbacks of aerosols on the SST evolution that could change the surface fluxes. However, due to the large heat capacity of the ocean, we do not expect the SST to dramatically change over the two days simulations.

For comparing the outgoing longwave flux from the simulations and observations we use imager data from the SEVIRI instrument onboard the Meteosat Second Generation (MSG) geostationary satellite (Aminou, 2002). The outgoing longwave flux is calculated using the Optimal Retrieval for Aerosol and Cloud (ORAC) algorithm (Sus et al. 2017; McGarragh, et al. 2017). Cloud optical (thickness, effective radius, water path) and thermal (cloud top temperature and pressure) properties are retrieved from ORAC using an optimal estimation-based approach. These retrievals and reanalysis profiles of temperature, humidity and ozone are then ingested into BUGSrad, a two-stream correlated-k broadband flux algorithm (Stephens et al., 2001) that outputs the fluxes at the top and bottom of the atmosphere and shown to have excellent agreement when applied to both active (CloudSat) and passive (Advanced Along Track Scanning Radiometer) satellite sensors compared to Clouds and the Earth's Radiant Energy System (Henderson et al. 2013; Stengel et al. 2019). In addition, off-line sensitivity radiative transfer tests using vertical profiles from our model were conducted with BUGSrad to identify the source of the differences in fluxes between clean and polluted conditions.

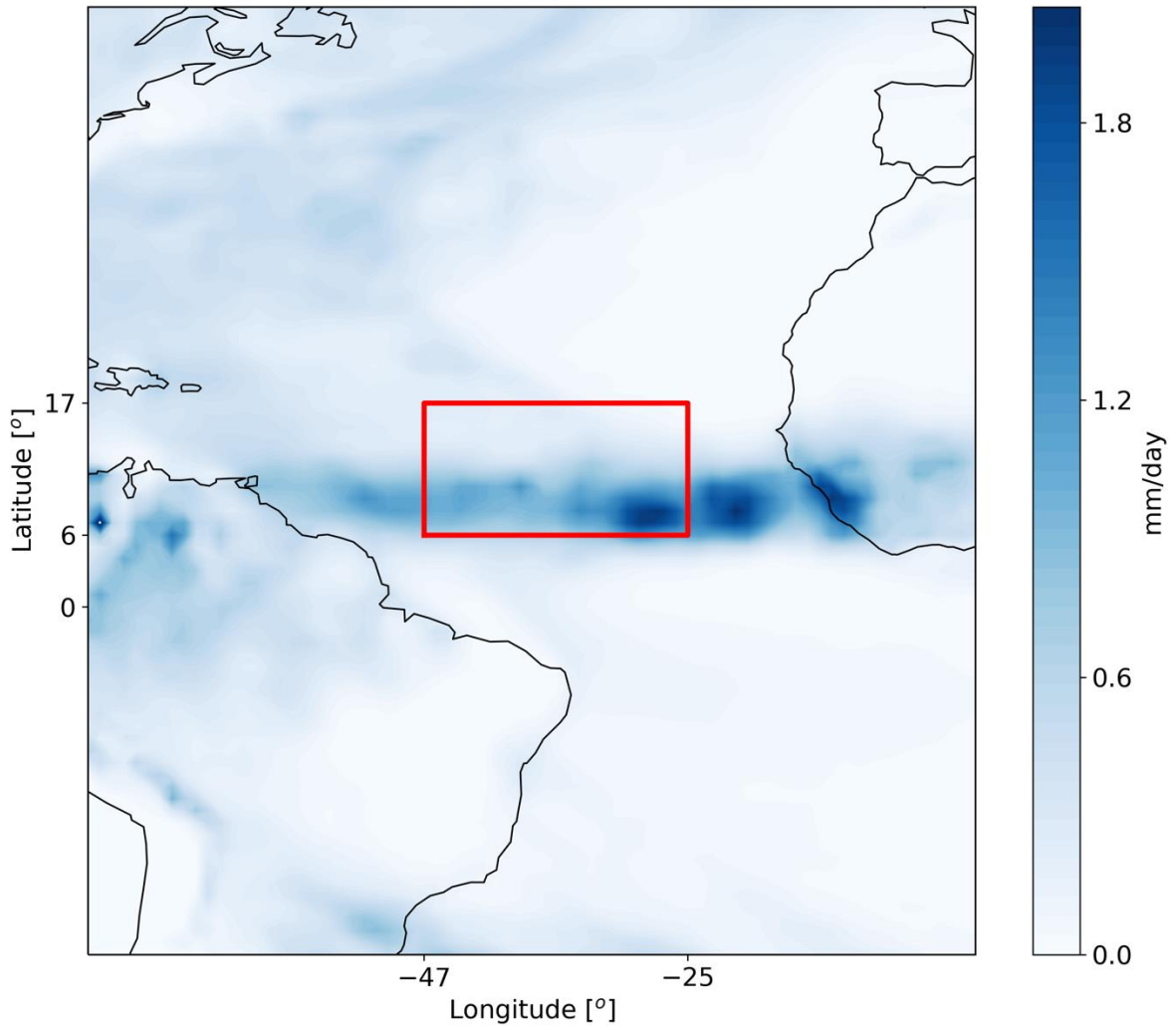

Figure 1. Domain of the ICON simulations (red rectangle) overlaid on the August 2016 ECMWF era-interim reanalysis (Dee et al., 2011) mean precipitation rate.

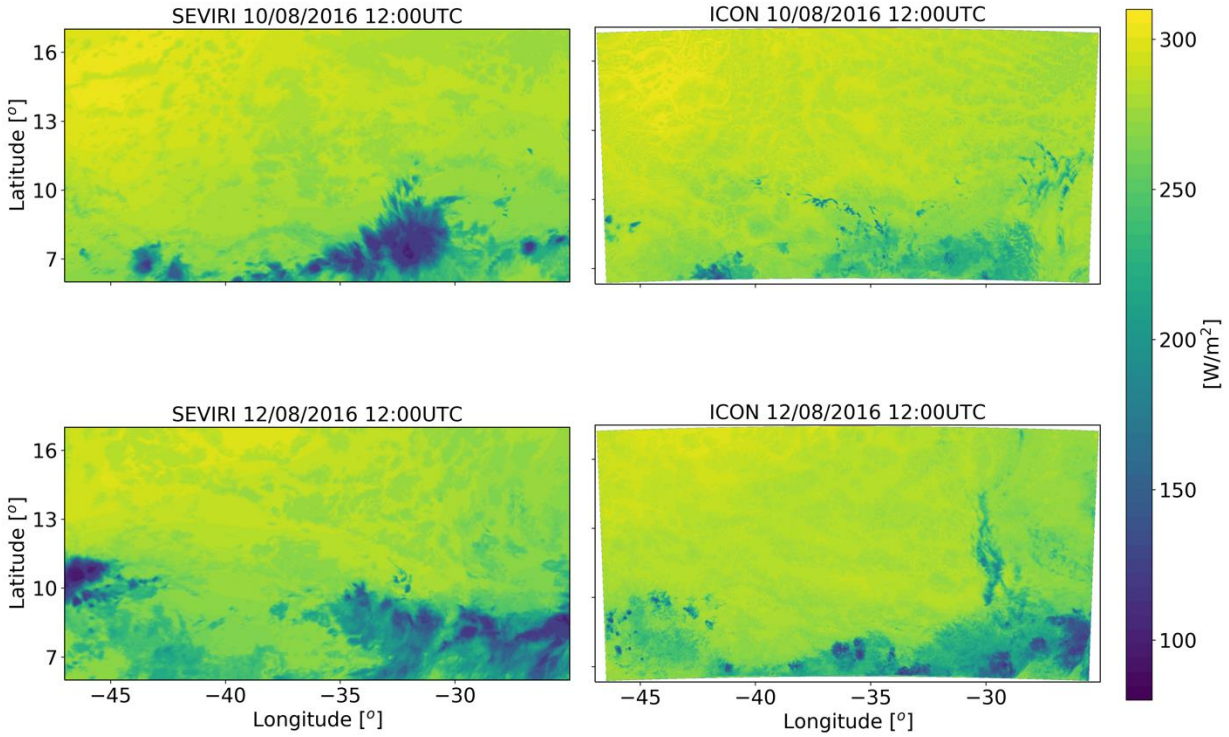

Figure 2. Outgoing longwave flux at the top of atmosphere at the initial stage (upper row) and the last stage (lower row – each average over 30 minutes) of the simulation of the shallow-cloud dominated case (10-12/08/2016) from geo-stationary satellite (SEVIRI-MSG – right column) and the ICON model simulation with CDNC of 20 cm^{-3} (left column).

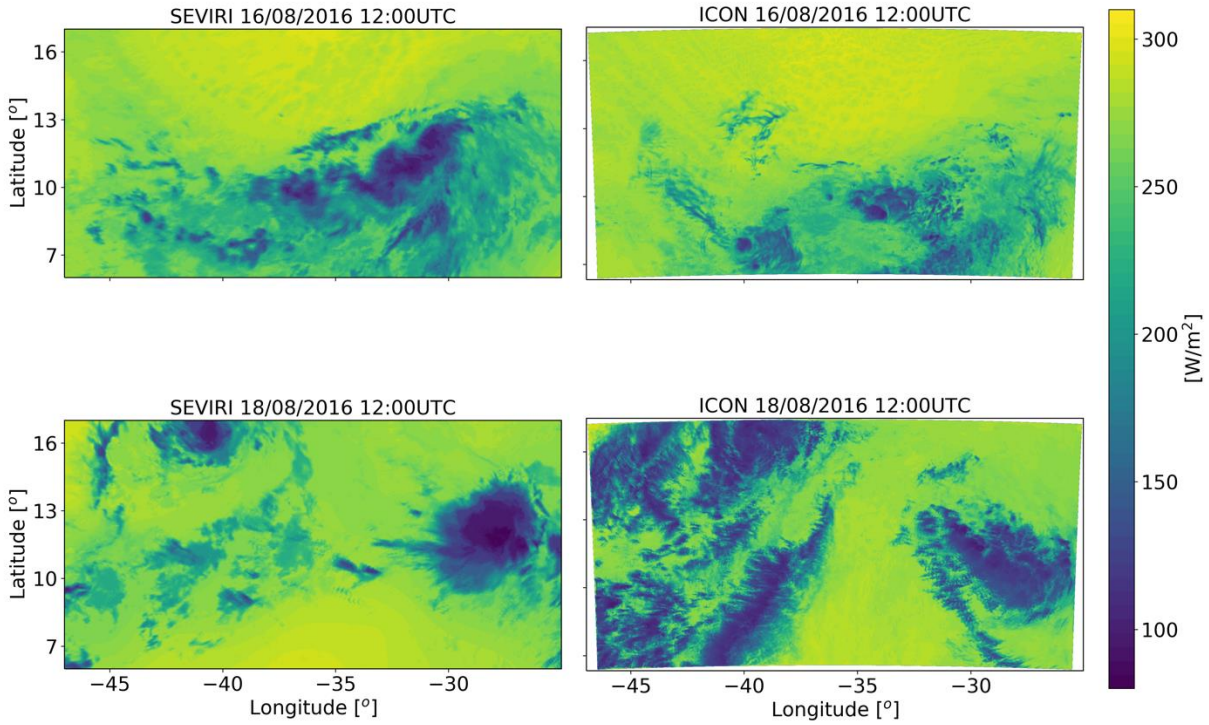

Figure 3. similar to Figure 2 but for the deep-cloud dominated case (16-18/08/2016).

Results

Shallow-cloud dominated case -10-12/08/2016

We start with energy budget analysis of the shallow-cloud dominated case base simulations (CDNC = 20 cm^{-3}). Figure 4 presents the time mean (over the two days simulation) of the different terms of the energy budget (Equation 1). As expected, *LP* dominates the warming of the atmosphere while Q_R dominate the cooling. The sensible heat flux (Q_{SH}) is positive (act to warm the atmosphere) but it is an order of magnitude smaller than the *LP* and Q_R magnitudes. In this shallow-cloud dominated case the radiative cooling of the atmosphere is significantly larger than the warming due to precipitation (mean of -114.7 W/m^2 compared to 90.1 W/m^2), hence the energy imbalance (R) is negative. Negative R means that there must be some convergence of dry static energy into the domain and/or decrease in the storage term, in this case it is mostly due to convergence of dry static energy.

We note that there is a significant difference in the spatial distribution of *LP* and Q_R (Jakob et al., 2019). While the Q_R is more uniformly distributed, the *LP* is mostly concentrated at the south part of the domain (where the deep convective clouds are formed) and it has a dotted structure. Locally, at the core of a deep convective clouds, the *LP* contribution can reach a few 1000 W/m^2 (1 mm/hr of precipitation is equivalent to 628 W/m^2), however, the vast majority of the domain

contributes very little in terms of *LP*. Q_R also presents some spatial structure in which there is a weak atmospheric cooling at the south part of the domain (the region of the deep convective clouds) and a strong cooling at the reset of the domain.

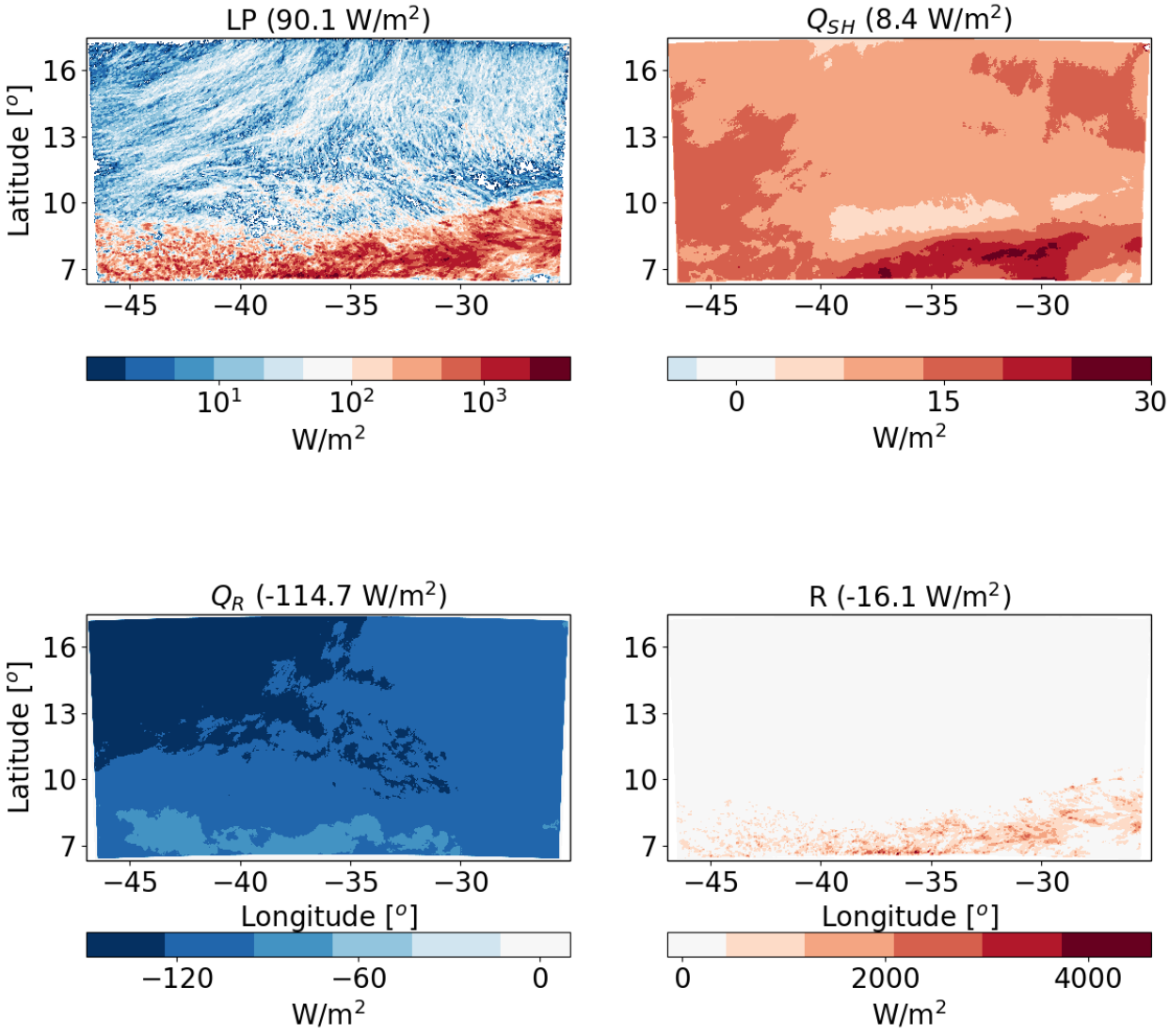

Figure 4. Spatial distribution of the time mean of the different terms of the energy budget for the ICON simulation of the shallow-cloud dominated case (10-12/08/2016) with CDNC = 20 cm^{-3}. The terms that appear here are: *LP* - latent heat by precipitation, Q_{SH} - sensible heat flux, Q_R - atmospheric radiative warming, and R – the energy imbalance. The domain and time-mean value of each term appears in parenthesis.

For understanding the spatial structure of Q_R, next we examine the spatial distribution of the LW and SW radiative fluxes at the TOA and surface (Fig. 5). We note that the smaller radiative cooling in the region of deep clouds in the south of the domain is mostly contributed by a decrease in F_{LW}^{TOA}. The SW fluxes also demonstrate a strong south-north gradient, as the deep

convective clouds in the south are more reflective than the shallow trade cumulus (with the lower mean cloud fraction) in the rest of the domain.

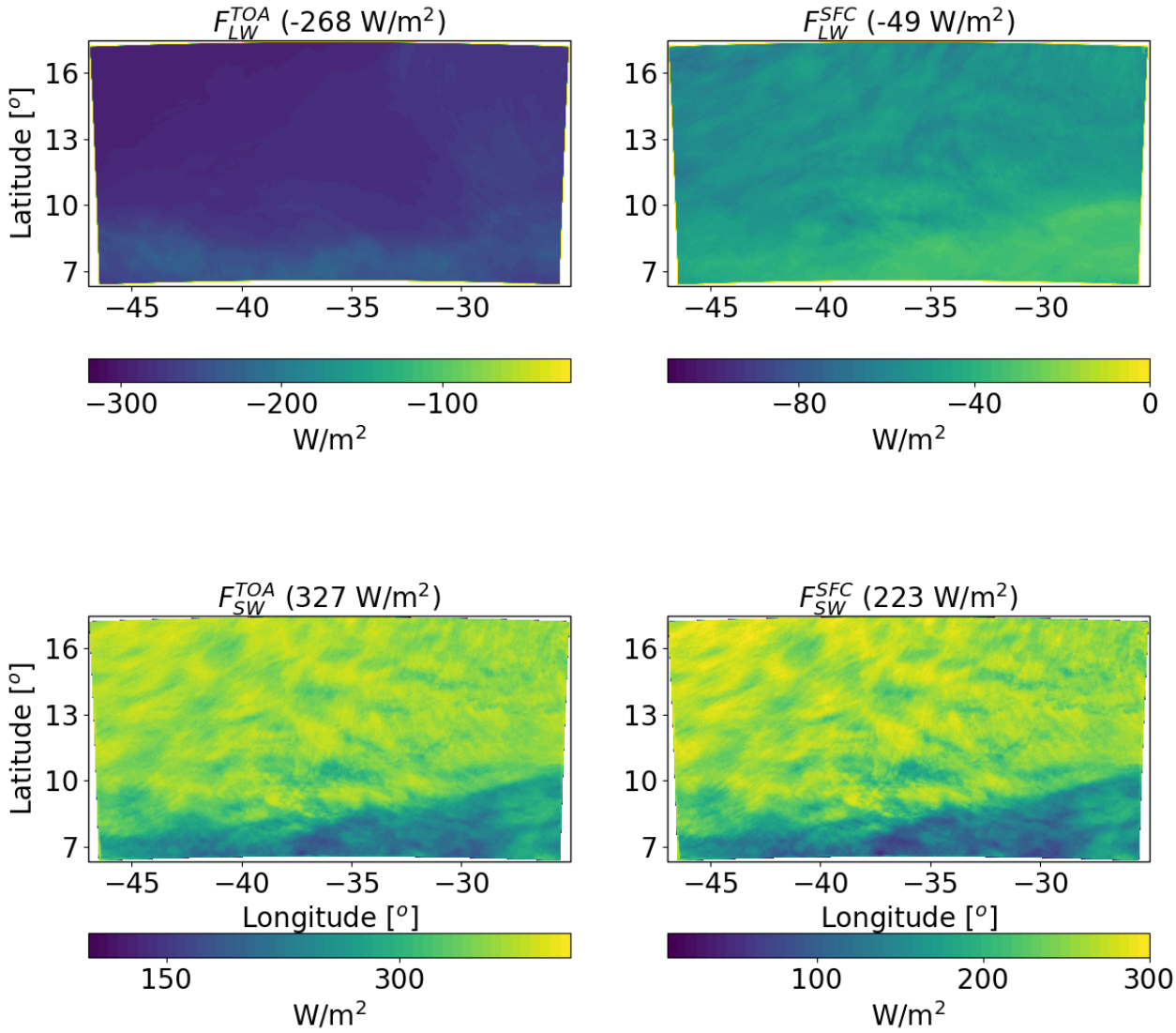

Figure 5. Spatial distribution of ICON simulated time-mean longwave (LW) and shortwave (SW) radiation fluxes at the top of atmosphere (TOA) and surface (SFC) for a simulation of the shallow-cloud dominated case (10-12/08/2016) with CDNC = 20 cm^{-3}. The domain and time mean value of each term appears in parenthesis.

Response to aerosol perturbation – shallow-cloud dominated case

Next, we analyse the response of the atmospheric energy budget of this case to perturbations in CDNC. Figure 6 presents the differences in the different terms of the energy budget between a

polluted simulation (CDNC = 200 cm^{-3}) and a clean simulation (CDNC = 20 cm^{-3}). It demonstrates that the *LP* differences between the different CDNC scenarios contribute 5.1 W/m^2 less to warm the atmosphere in the polluted vs. the clean simulation. We note that this apparently large effect is caused by a small, non-statistically significant, precipitation difference (~0.4 mm over the two days of simulation - see Fig. 8 below). The strong sensitivity of the atmospheric energy budget to small precipitation changes (recalling that 1 mm/hr is equivalent to 628 W/m^2) exemplifies the caution one needs to take when looking on precipitation response in terms of energy budget perspective. The Q_R differences lead to relative warming of the atmosphere of the polluted case compared to the clean case by 1.6 W/m^2. We note that most of the Q_R differences are located in the south-west part of the domain. The Q_{SH} changes counteracts 1.4 W/m^2 of the atmospheric warming by Q_R and so the end result is a deficit of 4.8 W/m^2 in the atmospheric energy budget in the polluted simulation compared to the clean simulation. The decrease in the Q_{SH} is driven by an increase in the near surface air temperature (see Fig. 8).

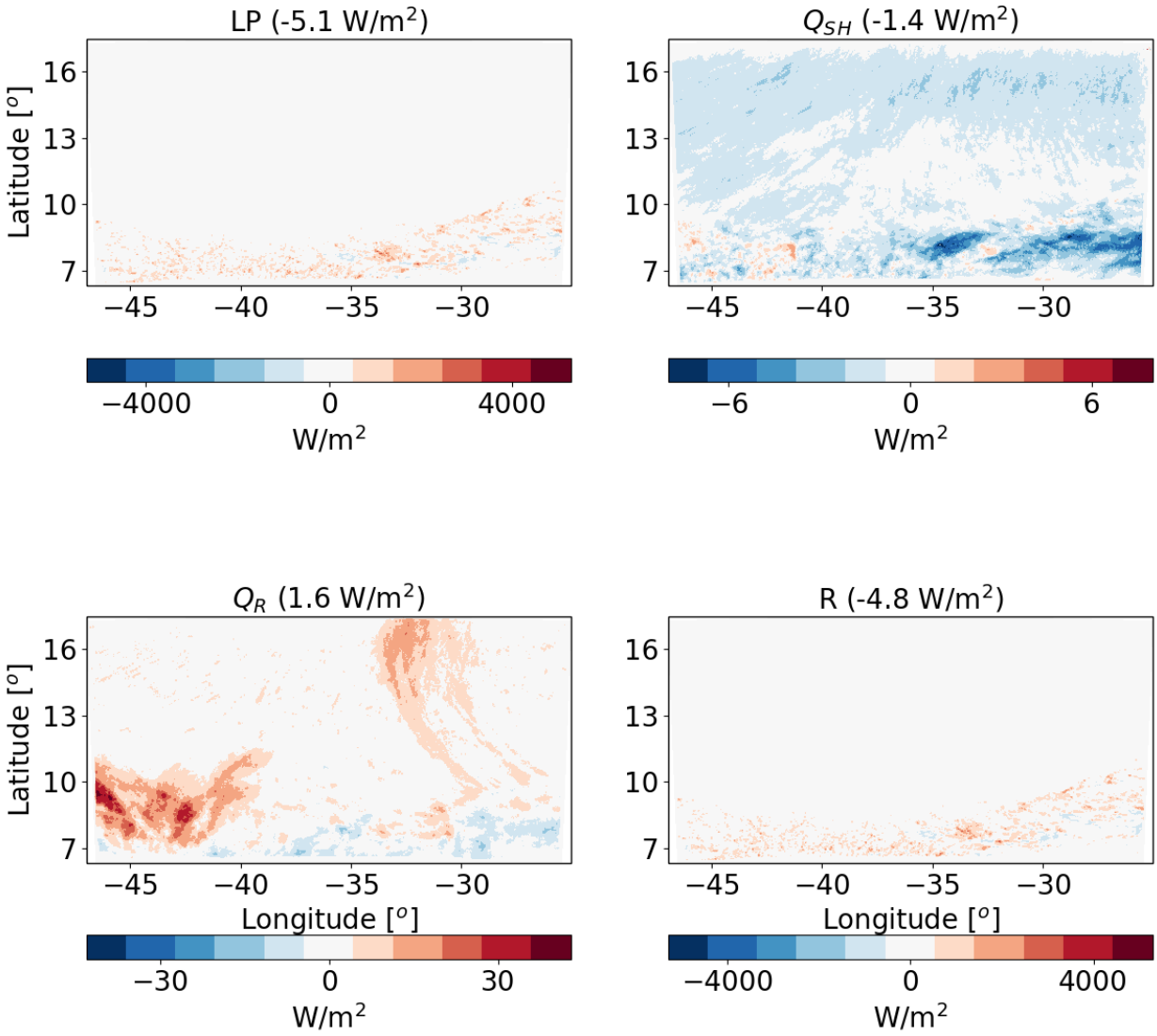

Figure 6. The differences between polluted (CDNC = 200 cm^{-3}) and clean (CDNC = 20 cm^{-3}) ICON simulations of the time-mean terms of the energy budget for the shallow-cloud dominated case (10-12/08/2016). The terms that appears here are: *LP* - latent heat by precipitation, Q_{SH} - sensible heat flux, Q_R - atmospheric radiative warming, and R – the energy imbalance. The domain and time mean value of each term appears in parenthesis.

To understand the response of Q_R to the CDNC perturbation, we next examine the response of the different radiative fluxes. Figure 7 demonstrates that most of the relative atmospheric radiative heating in the polluted case compared to the clean case is contributed by changes in the F_{LW}^{TOA} fluxes. The changes in F_{LW}^{SFC} are an order of magnitude smaller. The SW fluxes change both at the TOA and SFC are larger than the F_{LW}^{TOA} changes, however, in terms of the atmospheric energy budget, they almost cancel each other out and the net SW atmospheric effect is only -0.9 W/m^2. Most of the reduction in SW fluxes (both at TOA and the surface) comes from the deep convective regions in the south of the domain while the shallow cloud regions experience some

increase in SW fluxes. This can be attributed to the increase in deep convective cloud fraction and a decrease in the shallow cloud fraction with the increase in CDNC (see Fig. 9 below). The TOA net radiative effect for the entire system (as opposed to the atmospheric energy budget that take into consideration the surface radiative fluxes changes) is about -5.2 W/m^2.

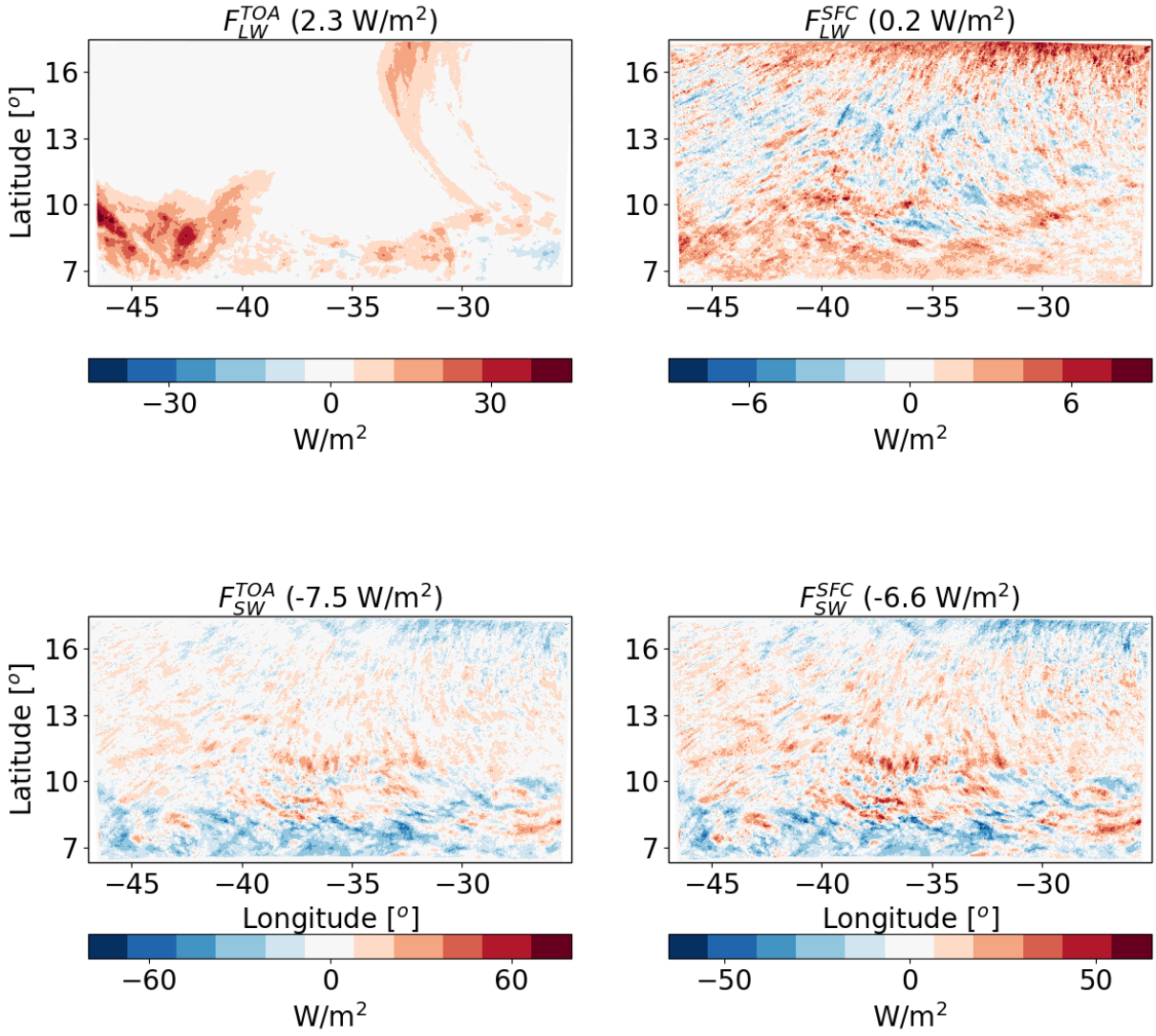

Figure 7. The differences between polluted (CDNC = 200 cm^{-3}) and clean (CDNC = 20 cm^{-3}) ICON simulations of the time mean radiative longwave (LW) and shortwave (SW) fluxes at the top of atmosphere (TOA) and surface (SFC) for the shallow-cloud dominated case (10-12/08/2016). The domain and time mean value of each term appears in parenthesis.

The differences in the energy (Fig. 6) and radiation (Fig. 7) budgets between the clean and polluted cases shown above, could be explained by the differences in the cloud mean properties. Figure 8 presents the time evolution of some of the domain mean properties while Fig. 9 presents time and horizontal mean vertical profiles. To examine the robustness of the trends we add here

two more CDNC cases of 100 and 500 cm^{-3} (on top of the two that were examine above – 20 and 200 cm^{-3}). Figure 8 demonstrates that the domain mean cloud fraction (CF) generally decreases with the increase in CDNC (except for the first ~10 hours of the simulations). Examining the vertical structure of the CF response (Fig. 9), demonstrates that with the increase in CDNC there is a reduction in the low level (below 800 mb) CF concomitantly with an increase in CF at the middle and upper troposphere. The differences in rain rate between the different simulations are small. However, both the liquid water path (LWP) and the ice water path (IWP) show a consistent increase with CDNC. Accordingly, also the total water path (TWP), which is the sum of the LWP and the IWP, substantial increases with CDNC. The vertical profiles of the different hydrometers (Fig. 9) indicate, as expected, that the cloud droplet mass mixing ration (qc - droplet with radius smaller than 40 μm) increases with CDNC, while the rain mass mixing ratio (qr - drops with radius larger than 40 μm) decreases due to the shift in the droplet size distribution to smaller sizes under larger CDNC conditions. As this case is dominated by shallow clouds, there exists only a comparably small amount of ice mixing ration (qi) (c.f. Fig. 17), but its concentration increases with the CDNC increase. The combined effect of the increase in CDNC is to monotonically increase the total water mixing ratio (qt) above 800 mb (Fig. 9). The relative increase in qt with CDNC becomes larger at higher levels.

The increase in cloud water with increasing CDNC can explain both the reductions in the net downward SW fluxes (both at TOA and surface) and the decrease in outgoing LW flux at TOA (Fig. 7), as it results in more SW reflection concomitantly with more LW trapping in the atmosphere (Koren et al., 2010). Another contributor to the SW flux reduction (more reflectance) at the TOA is the Twomey effect (Twomey, 1977), while, the decrease in the low-level CF compensates some of this effect. Here we present the outcome of these contradicting effects on the SW fluxes, which shows a reduction at both the TOA and surface (Fig. 7). For estimating the relative contribution of the Twomey effect compare to the cloud adjustments (CF and TWP effects) to the SW flux changes, we have re-run the simulations with the Twomey effect turned off (the radiation calculations do not consider the changes in effective radius between the different simulations). It demonstrates that without the Twomey effect the TOA SW difference is only -1.7 W/m^2 as compared to -7.5 W/m^2 with the Twomey effect, demonstrating the predominant role of the Twomey effect. For estimating the relative contribution of the changes in CF and water content to the SW flux changes we have conducted off-line radiative transfer sensitivity tests. To quantify the water content radiative effect, we feed the same CF vertical profile from the model into the offline radiative transfer model BUGSrad, while allowing the

water content vertical profile to change (and visa versa to compute the CF radiative effect). This approach demonstrates that the contribution from the small reduction in CF is negligible compared to the increased SW reflectance caused by the increased water content (the effect of the reduction in CF compensate only about 1% of the effect of the increase in the water content).

We also note a monotonic increase in the near surface temperature with CDNC (see also Fig. 10 below). This trend can be explained by warm rain suppression with increasing CDNC that leads to less evaporative cooling (see the decrease in the total amount of water mass mixing ration just above the surface in Fig. 9, (Dagan et al., 2016; Albrecht, 1993; Seigel, 2014; Seifert and Heus, 2013; Lebo and Morrison, 2014)). In addition, it was shown that under polluted conditions the rain drops below cloud base are larger, hence evaporating less efficiently (Lebo and Morrison, 2014; Dagan et al., 2016). The increase in the near surface temperature drives the decrease in the Q_{SH} (Fig. 6).

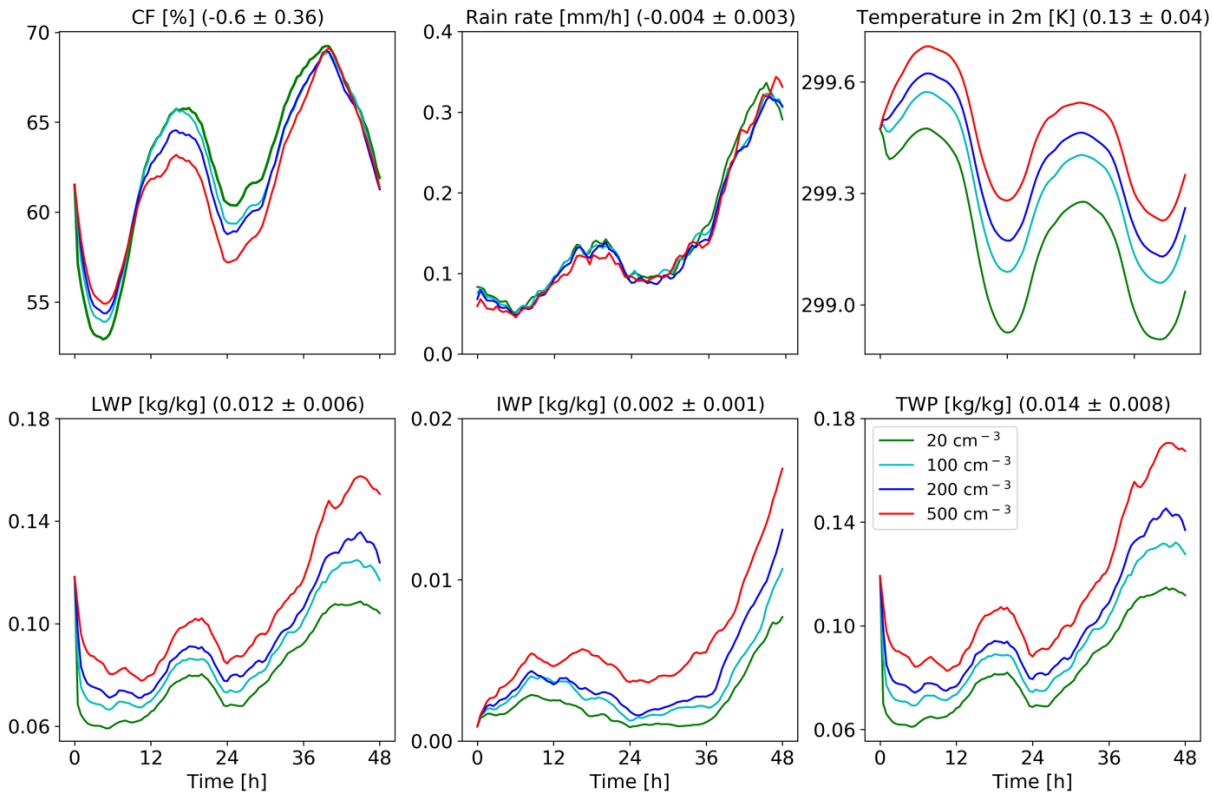

Figure 8. Domain average properties as a function of time for the different CDNC simulations for the shallow-cloud dominated case. The properties that are presented here are: cloud fraction (CF), rain rate, temperature in 2 m, liquid water path (LWP – based on the cloud water mass, excluding the rain mass for consistency with satellite observations), ice water path (IWP) and total water path (TPW = LWP + IWP). For each property, the mean difference between all combinations of simulations, normalized to a factor 5 increase in CDNC, and its standard deviation appear in parenthesis.

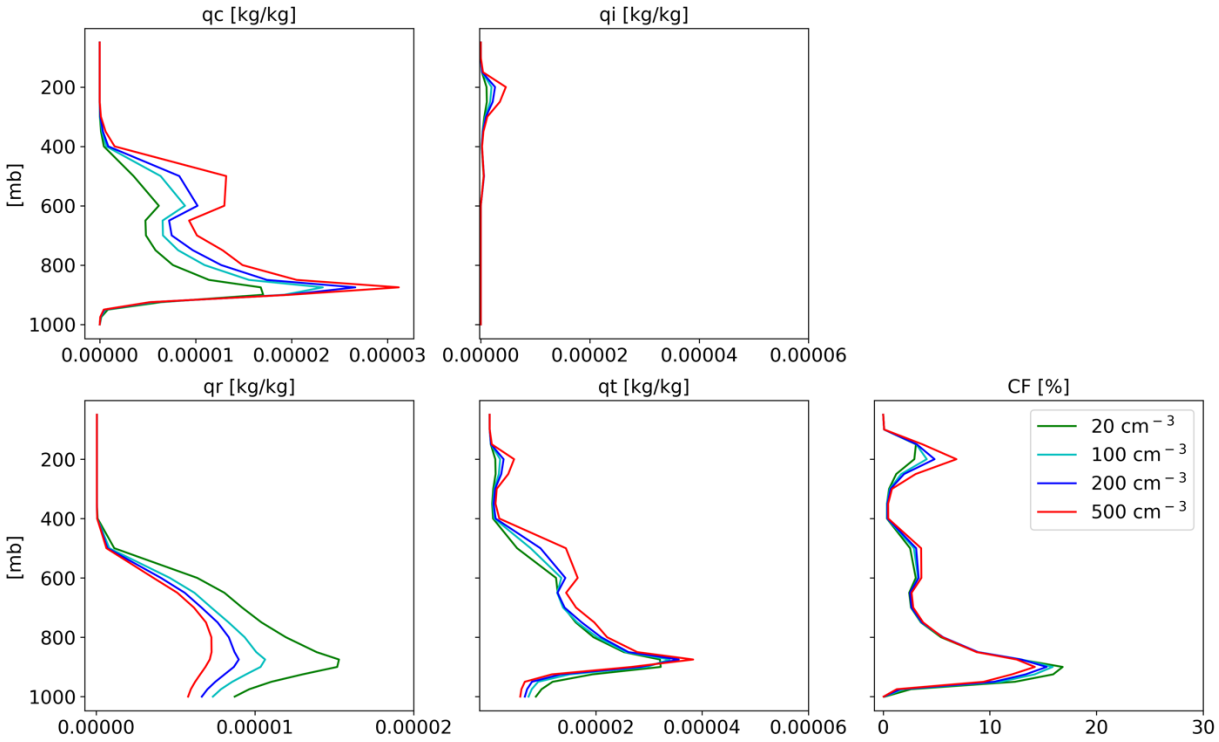

Figure 9. Domain and time average vertical profiles for the different CDNC simulations for the shallow-cloud dominated case. The properties that are presented here are: cloud droplet mass mixing ratio (qc – for clouds' droplets with radius smaller than 40 μm), ice mass mixing ratio (qi), rain mass mixing ratio (qr - for clouds' drops with radius larger than 40 μm), total water mass mixing ratio (qt = qc+qi+qr), and cloud fraction (CF). The x-axis ranges are identical as for the deep-cloud dominated case – Fig. 17.

In addition to the clouds' effect on the radiation fluxes, changes in humidity could also contribute (Fig. 10). We note that increase in CDNC leads to increase in relative humidity (RH) and specific humidity (qv) at the middle and upper troposphere without a significant temperature change. The increased humidity at the upper troposphere would act to decrease the outgoing LW flux, similar to the effect of the increased ice content in the upper troposphere (Fig. 9). However, sensitivity studies with off-line radiative transfer calculations using BUGSrad demonstrate that the vast majority (more than 99%) of the different in F_{LW}^{TOA} between clean and polluted conditions emerges from the cloudy skies (rather than clear-sky), suggesting that the effect of the increased ice content at the upper troposphere dominates.

Both the increase in water vapor and ice content in the upper troposphere are driven by an increase in upward water (liquid and ice) mass flux with increasing CDNC (Fig. 11). An increase

386 in mass flux could be caused by an increase in vertical velocities and/or by an increase in cloud
387 (or updraft) fraction and/or by an increase in cloud water content. In our case, the increases in
388 mass flux is driven partially by the small increase in vertical velocity (especially for updraft
389 between 5 and 10 m/s – Fig. 11), partially by the small increase in cloud faction at this level (Fig.
390 9) and mostly due to the larger water mass mixing ratio (Fig. 9) that leads to an increase in mass
391 flux even for a given vertical velocity. The increased relative humidity at the upper troposphere,
392 further increases the ice particle lifetime at these levels (in addition to the microphysical effect
393 (Grabowski and Morrison, 2016)) as the evaporation rate decreases. In addition, the differences
394 in the thermodynamics evolution between the different simulations (Fig. 10) demonstrate drying
395 and warming of the boundary layer with increasing CDNC, due to reduction in rain evaporation
396 below cloud base and deepening of the boundary layer (Dagan et al., 2016; Lebo and Morrison,
397 2014; Seifert et al., 2015; Spill et al., 2019). The drying of the boundary layer could explain the
398 reduction in the low cloud fraction (Fig. 9 (Seifert et al., 2015)).

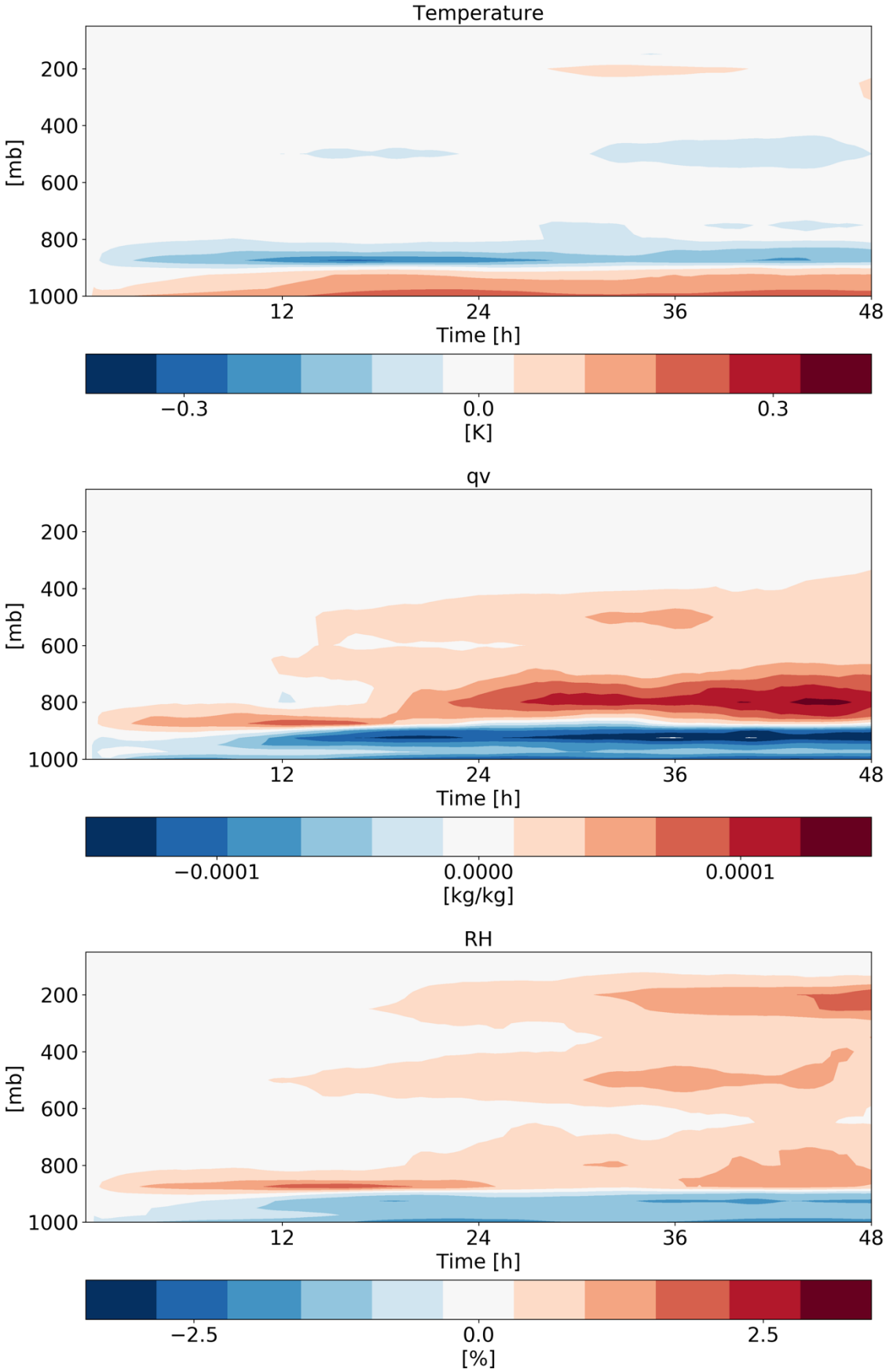
Temperature
200
400
600
800
1000
[mb]
12
24
36
48
Time [h]
−0.3
0.0
0.3
[K]
qv
200
400
600
800
1000
[mb]
12
24
36
48
Time [h]
−0.0001
0.0000
0.0001
[kg/kg]
RH
200
400
600
800
1000
[mb]
12
24
36
48
Time [h]
−2.5
0.0
2.5
[%]

399

Figure 10. Time-height diagrams of the differences in the domain mean temperature, specific humidity (qv) and relative humidity (RH) vertical profiles between polluted (CDNC = 200 cm^{-3}) and clean (CDNC = 20 cm^{-3}) simulations for the shallow-cloud dominated case (10-12/08/2016).

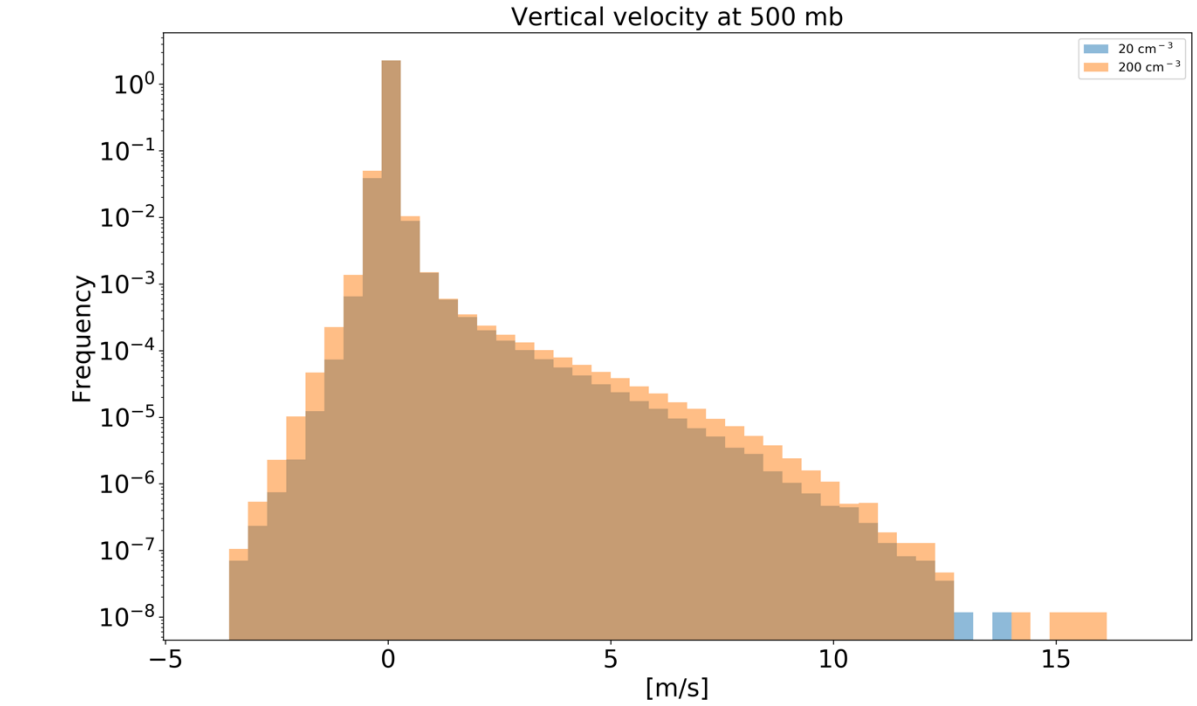

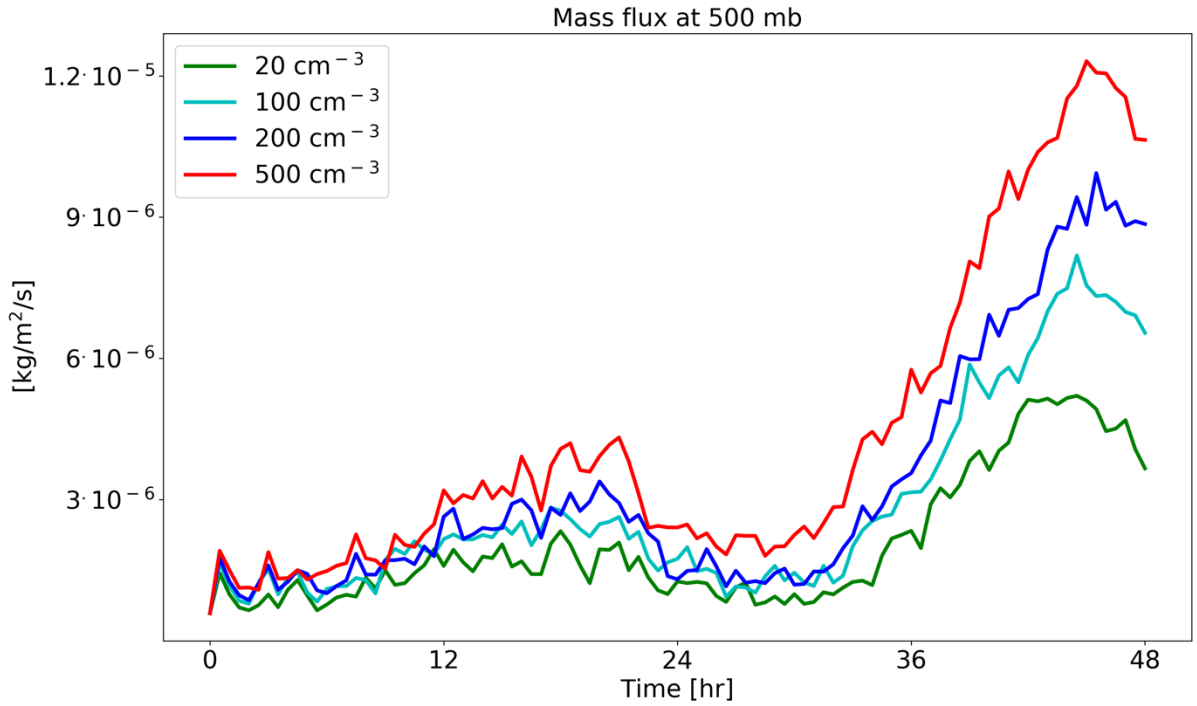

Figure 11. histograms of ICON simulated vertical velocity at the level of 500 mb for a clean (CDNC = 20 cm^{-3}) and polluted (CDNC = 200 cm^{-3}) simulations (upper), and the time evolution of the net upwards water (liquid and ice) mass flux (lower) for the different CDNC simulations for the shallow-cloud dominated case

(10-12/08/2016). The 500 mb level is chosen as it represents the transition between the warm part to the cold part of the clouds. In the histogram only two simulations are presented for clarity.

Deep-cloud dominated case -16-18/08/2016

Next, we analyse the atmospheric energy budget for the deep-cloud dominated case (Fiona tropical storm – Fig. 12). As opposed to the shallow-cloud dominated case, in this case the *LP* contribution dominates over the radiative cooling and hence the energy imbalance R is positive and large, suggesting divergence of dry static energy out of the domain. This difference in the base line atmospheric energy budget between the different cases simulated here, enable an examination of the aerosol effect on the atmospheric energy budget under contrasting initial conditions. As in the shallow-cloud dominated case, the Q_R values varies between small values (especially at the regions that were mostly covered by deep clouds) to larger negative values (dominated at the regions that were coved by shallow clouds). The Q_{SH} is positive and an order of magnitude smaller than the Q_R and *LP*, similar to the shallow-cloud dominated case.

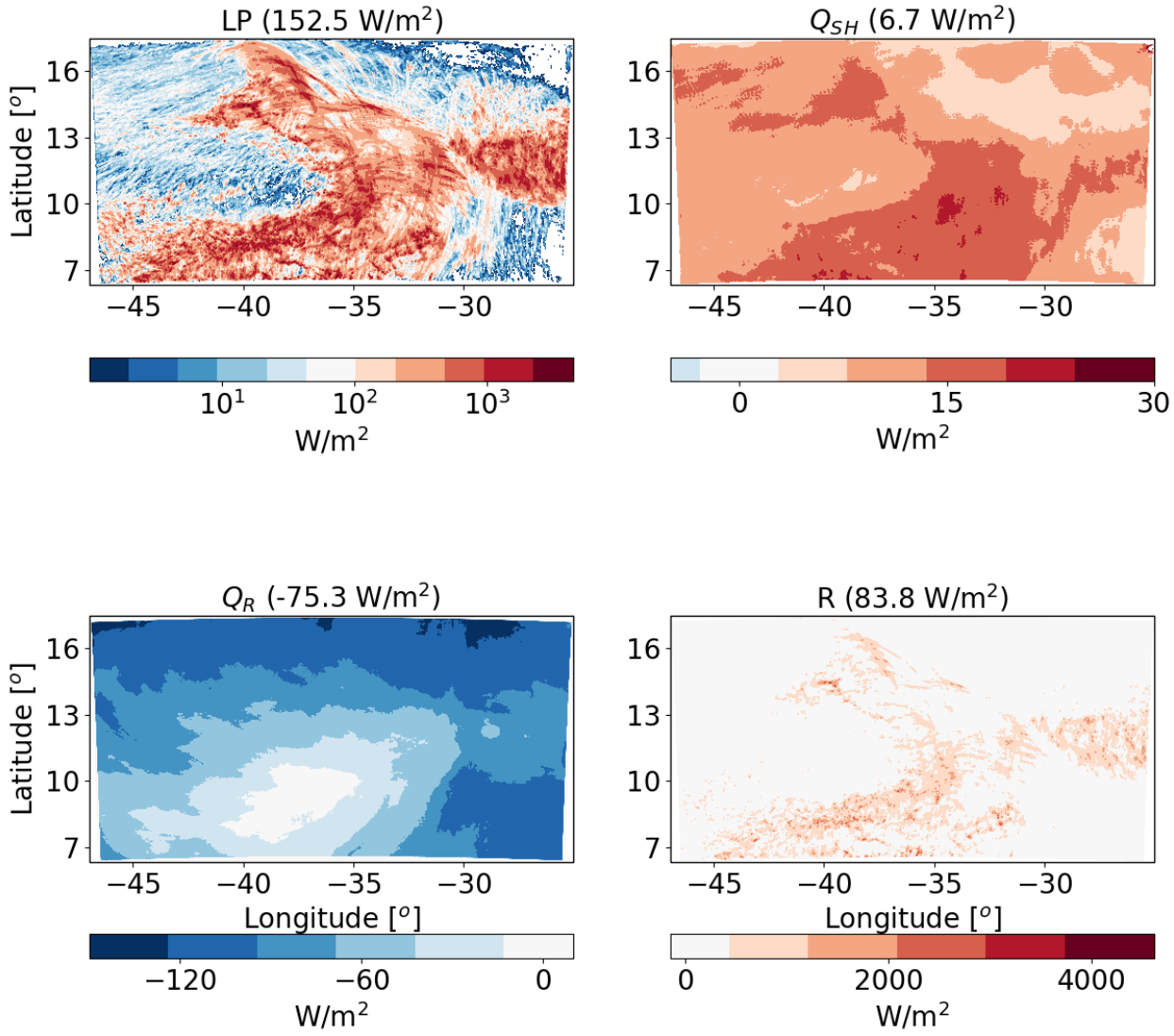

Figure 12. Spatial distribution of the time mean of the different terms of the energy budget for the ICON simulation of the deep-cloud dominated case (16-18/08/2016) with CDNC = 20 cm^{-3}. The terms that appear here are: *LP* - latent heat by precipitation, Q_{SH} - sensible heat flux, Q_R - atmospheric radiative warming, and R – the energy imbalance. The domain and time-mean value of each term appears in parenthesis.

Further examination of the radiative fluxes (Fig. 13) demonstrates again the resemblance in the spatial structure between Q_R and F_{LW}^{TOA}. As compared to the shallow-cloud dominated case, since the clouds are more opaque and cover larger fraction of the sky, there is a decrease in the magnitude of all fluxes (in different amount). For example, F_{SW}^{SFC} is lower by 41 W/m^2 (representing larger SW reflectance back to space) and the magnitude of F_{LW}^{TOA} by 47 W/m^2 as compare to the shallow-cloud dominated case. The combined effect of the radiative flux

differences between the two cases is a decrease of the atmospheric radiative cooling by 39.6 W/m^2 (-114.7 compare with -75.3 W/m^2 – see Figs. 5 and 13).

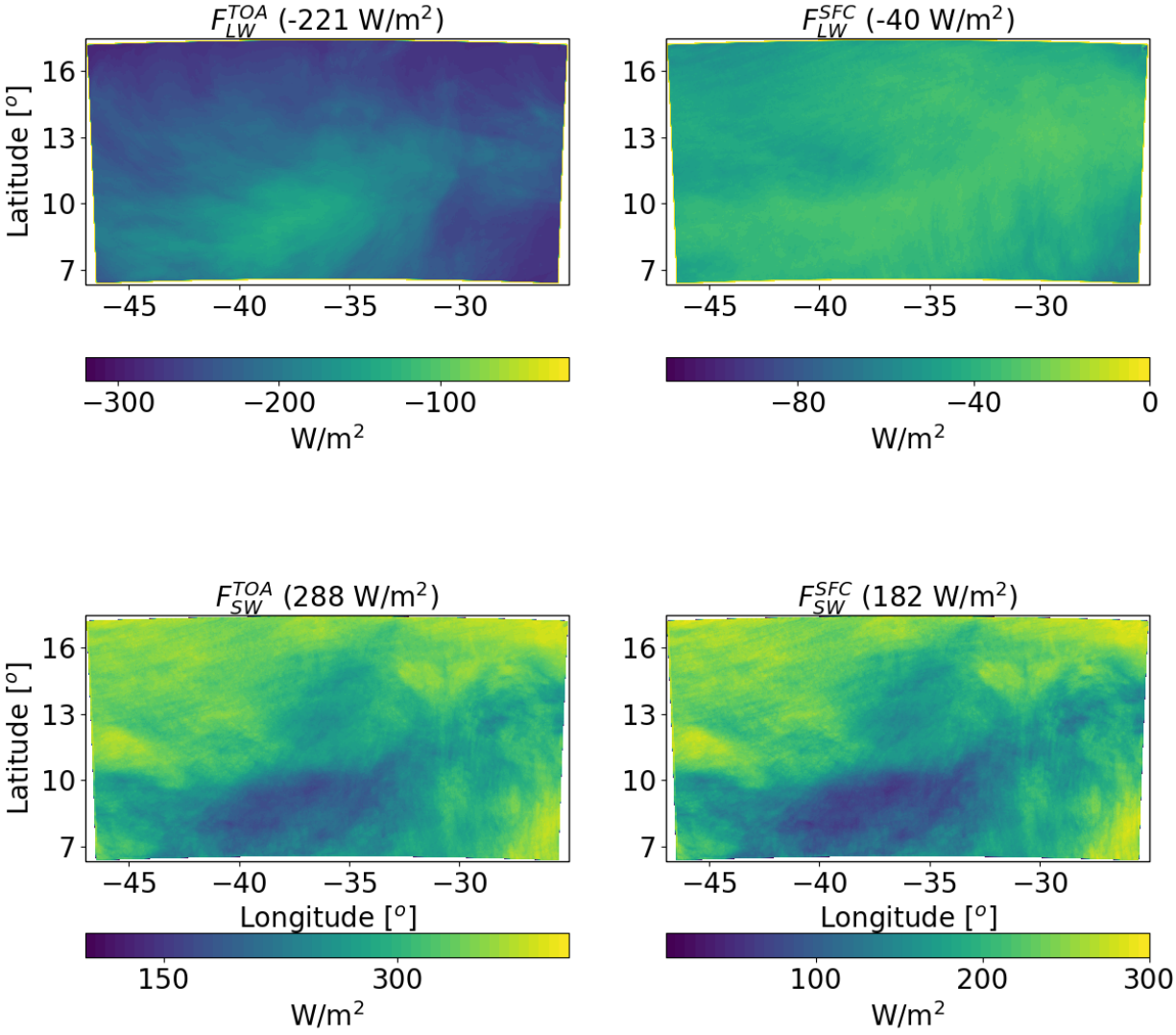

Figure 13. Spatial distribution of ICON simulated time-mean longwave (LW) and shortwave (SW) radiation fluxes at the top of atmosphere (TOA) and surface (SFC) for a simulation of the deep-cloud dominated case (16-18/08/2016) with CDNC = 20 cm^{-3}. The domain and time mean value of each term appears in parenthesis.

Response to aerosol perturbation – deep-cloud dominated case

For the deep-cloud dominated case, an increase in CDNC results in a decrease in *LP* by -0.3 W/m^2. Again, this difference is due to a non-statistically significant precipitation changes (see also Fig. 16 below). A similar Q_{SH} decrease as in the shallow-cloud dominated case is observed in the deep-clouds dominated case (see Figs. 14 and 6). The predominant difference in the

response between the two cases is in Q_R, which increases much more in the deep-cloud dominated case: 10.0 W/m^2 (Fig. 14) compared with 1.6 W/m^2 in the shallow-cloud dominated case (Fig. 6).

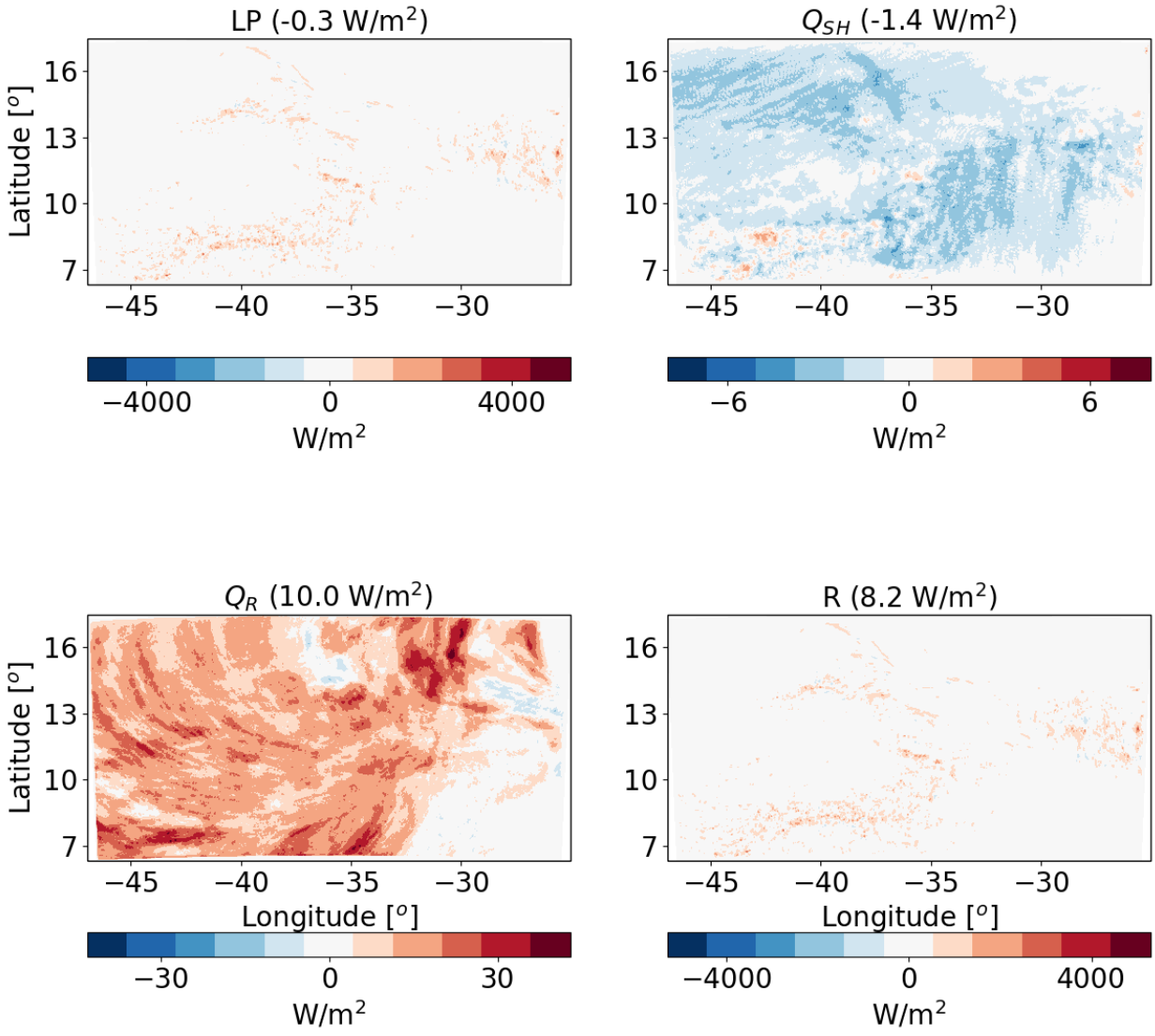

Figure 14. The differences between polluted (CDNC = 200 cm^{-3}) and clean (CDNC = 20 cm^{-3}) ICON simulations of the time-mean terms of the energy budget for the deep-cloud dominated case (16-18/08/2016). The terms that appears here are: *LP* - latent heat by precipitation, Q_{SH} - sensible heat flux, Q_R - atmospheric radiative warming, and R – the energy imbalance. The domain and time mean value of each term appears in parenthesis.

The large increase in Q_R is caused mostly by the increase in $\boldsymbol{F_{LW}^{TOA}}$ (which becomes less negative i.e. less outgoing LW radiation under polluted conditions – Fig. 15). The CDNC effect on $\boldsymbol{F_{LW}^{SFC}}$ has a much smaller magnitude. The SW fluxes changes are substantial (-14.1 W/m^2 at TOA and

-12.3 W/m^2 at the surface), however, in terms of the atmospheric energy budget, since clouds do not absorb much in the SW, the TOA and surface changes almost cancel each other out and the net effect is only ~1.8 W/m^2 atmospheric radiative cooling (which decrease some of the LW warming). The net TOA total (SW+LW) radiative flux change is about -1.9 W/m^2. The trends in the mean cloud properties (Figs. 16 and 17 below) can explain this large radiative response.

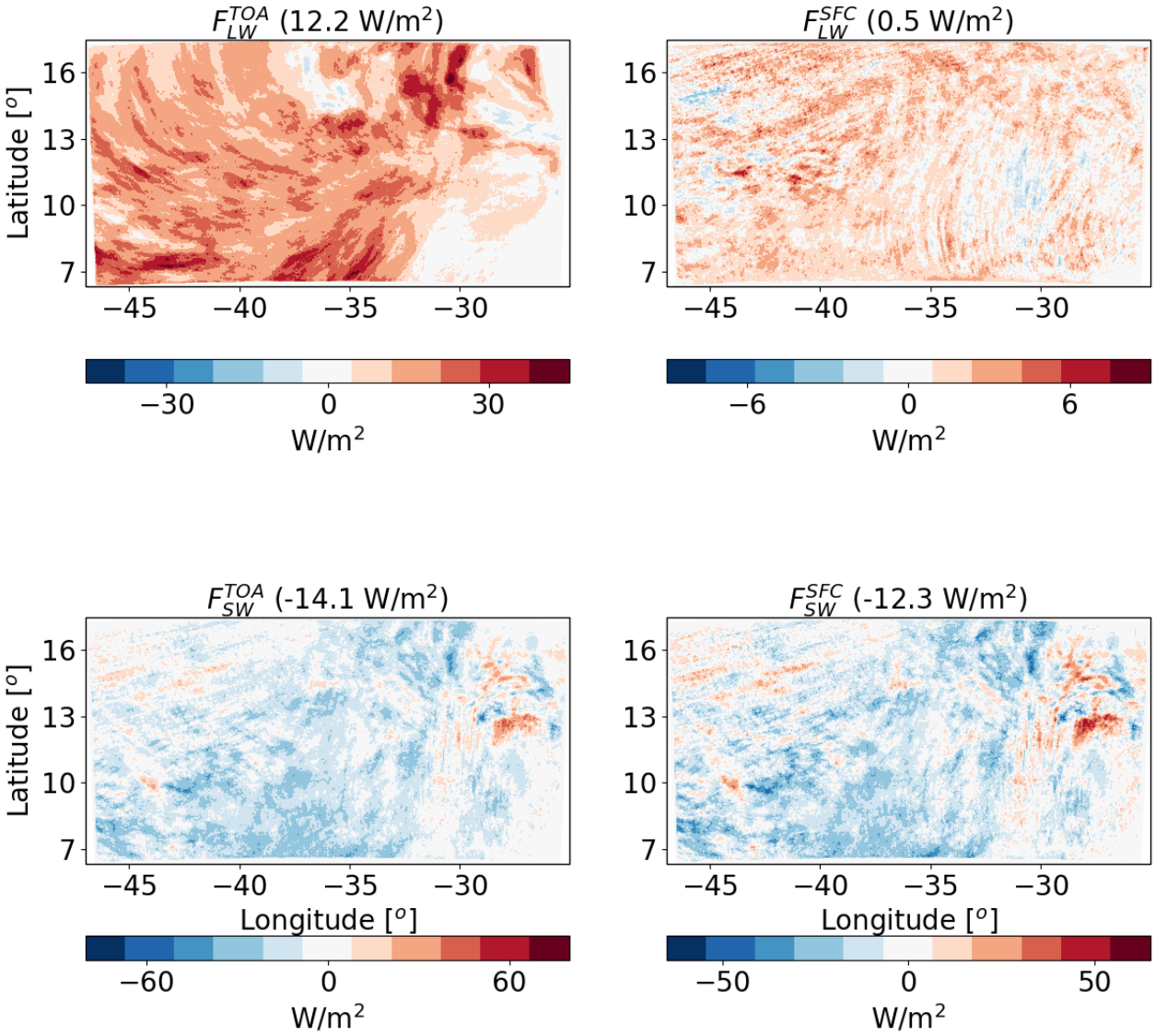

Figure 15. The differences between polluted (CDNC = 200 cm^{-3}) and clean (CDNC = 20 cm^{-3}) ICON simulations of the time mean radiative longwave (LW) and shortwave (SW) fluxes at the top of atmosphere (TOA) and surface (SFC) for the deep-cloud dominated case (16-18/08/2016). The domain and time mean value of each term appears in parenthesis.

Figure 16 presents some of the domain mean properties as a function of time for the deep-cloud dominated case. It demonstrates an increase in CF with CDNC which is more significant during the second day of the simulation. This is opposite to the CF reduction in the shallow-cloud dominated case (Fig. 8). It also demonstrates a very significant increase in LWP and, even more (in relative terms), in IWP and thus also in TWP. The increase in CF and water content can explain the decrease in SW fluxes both at TOA and surface (Fig. 15) as more SW is being reflected back to space. The larger SW reflection under increased CDNC is also contributed to by the Twomey effect (Twomey, 1977). Re-running the simulations without the Twomey effect result in 9.6 W/m^2 reduction in the TOA SW flux as compare to 14.1 W/m^2 with the Twomey effect on. We note that the relative role of the Twomey effect (compare to the cloud adjustments – CF and TWP) is larger in the shallow-cloud dominated case as compared to the deep-cloud dominated case (-14.1 W/m^2 and -9.6 W/m^2 for simulations with and without the Twomey effect in the deep-cloud dominated case, compare to -7.5 W/m^2 and -1.7 W/m^2 in the shallow-cloud dominated case, respectively). However, it should be noted that the Twomey effect due to changes in the ice particles size distribution was not considered. In this case, unlike in the shallow-cloud dominated case, the three contributions to the SW changes (CF, Twomey and LWP/IWP, e.g. (Goren and Rosenfeld, 2014)) all contribute to the SW flux reduction (Fig. 15 presents the results of all contributors). Off-line sensitivity tests demonstrate that the relative contribution of the water content and the CF to the increase in SW reflectance is roughly ¾ and ¼, respectively.

The vertical profile changes with CDNC (Fig. 17) demonstrate a consistent picture of a decrease in CF in low clouds and a significant increase in CF and liquid and ice content at the mid and upper troposphere. The CF increase at the upper troposphere, and especially the increase in the ice content, can explain the decrease in the outgoing LW radiation (Fig. 15). The increase in ice content at the upper troposphere is in agreement with recent observational studies (Gryspeerdt et al., 2018; Sourdeval et al., 2018; Christensen et al., 2016). Analysis of the upward water mass flux from the warm to the cold part of the clouds (at 500 mb) in the different simulations (Fig. 19), demonstrates a substantial increase with the increase in CDNC (Chen et al., 2017), which occurs due to the increase in the water content (Fig. 17) and the delay in the rain formation to higher levels (Heikenfeld et al., 2019), even without a large change in the vertical velocity or cloud fraction at this level (Fig.17). Similar to the shallow-cloud dominated case (Fig. 8), the near surface temperature monotonically increases with CDNC, while the effect on the mean rain rate is small.

The differences in the thermodynamic evolution between polluted and clean conditions for this case (Fig. 18), demonstrate the same trend as in the shallow-cloud dominated case (Fig. 10). Here again, we note an increase in the humidity at the mid and upper troposphere, that contribute to the reduction in the outgoing LW flux. The deepening, drying and warming of the boundary layer are observed in this case as well. Both the increase in humidity at the mid-upper troposphere and the deepening of the boundary layer (Seifert et al., 2015) could cause a reduction of the outgoing LW flux. To distinguished the effect of clouds and humidity at the different levels on the outgoing LW flux, we have conducted sensitivity off-line radiative transfer calculations using BUGSrad. As in the shallow-cloud dominated case, the difference in outgoing LW flux between clean and polluted conditions primarily emerges from the CDNC effect on clouds. The small remaining effect of the clear sky (~0.2 W/m^2) is contributed by the change in the humidity at the mid and upper troposphere rather than by the deepening of the boundary layer (which would lead to LW emission from lower temperatures and is expected to be more significant under lower free troposphere humidity conditions).

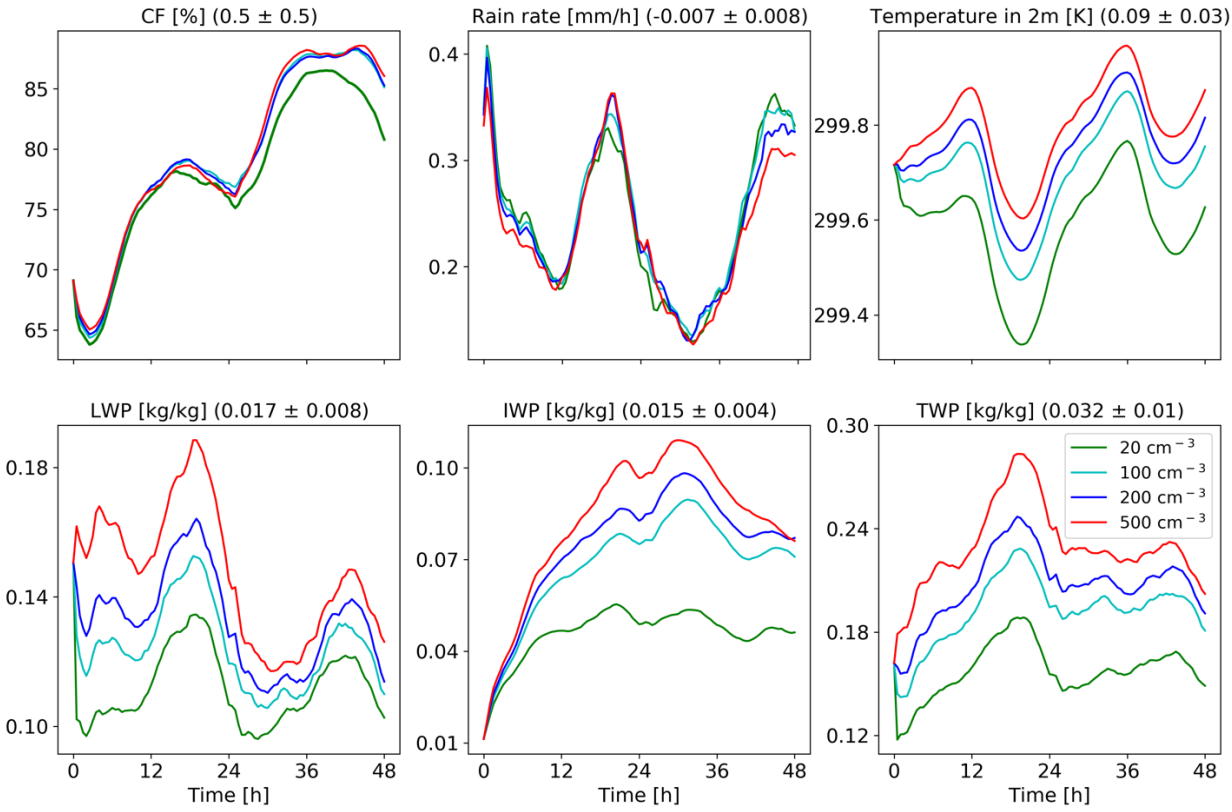

Figure 16. Domain average properties as a function of time for the different CDNC simulations for the deep-cloud dominated case. The properties that are presented here are: cloud fraction (CF), rain rate, temperature in 2 m, liquid water path (LWP – based on the cloud water mass, excluding the rain mass for consistency with satellite observations), ice water path (IWP) and total water path (TPW = LWP + IWP). For each

property, the mean difference between all combinations of simulations, normalized to a factor 5 increase in CDNC, and its standard deviation appear in parenthesis.

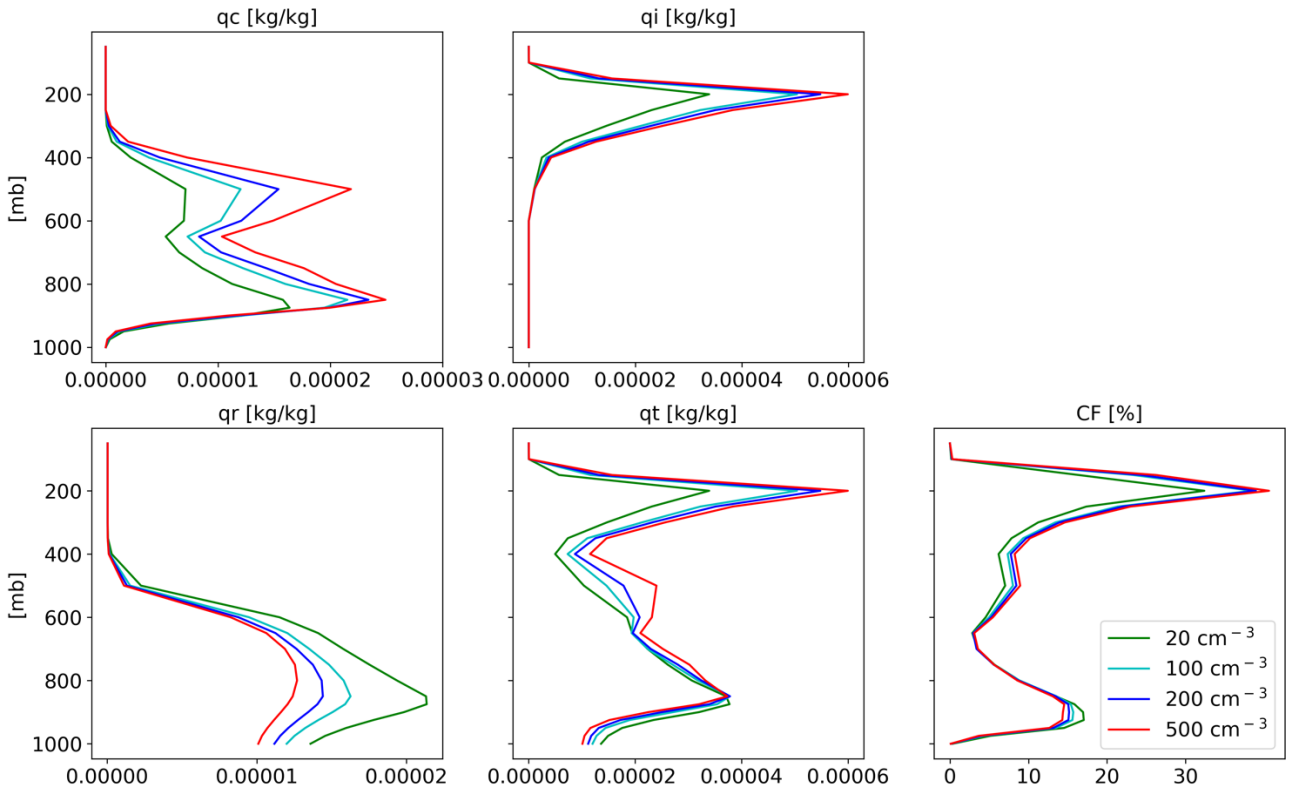

Figure 17. Domain and time average vertical profiles for the different CDNC simulations for the shallow-cloud dominated case. The properties that are presented here are: cloud droplet mass mixing ratio (qc – for clouds' droplets with radius smaller than 40 μm), ice mass mixing ratio (qi), rain mass mixing ratio (qr - for clouds' drops with radius larger than 40 μm), total water mass mixing ratio (qt = qc+qi+qr), and cloud fraction (CF).

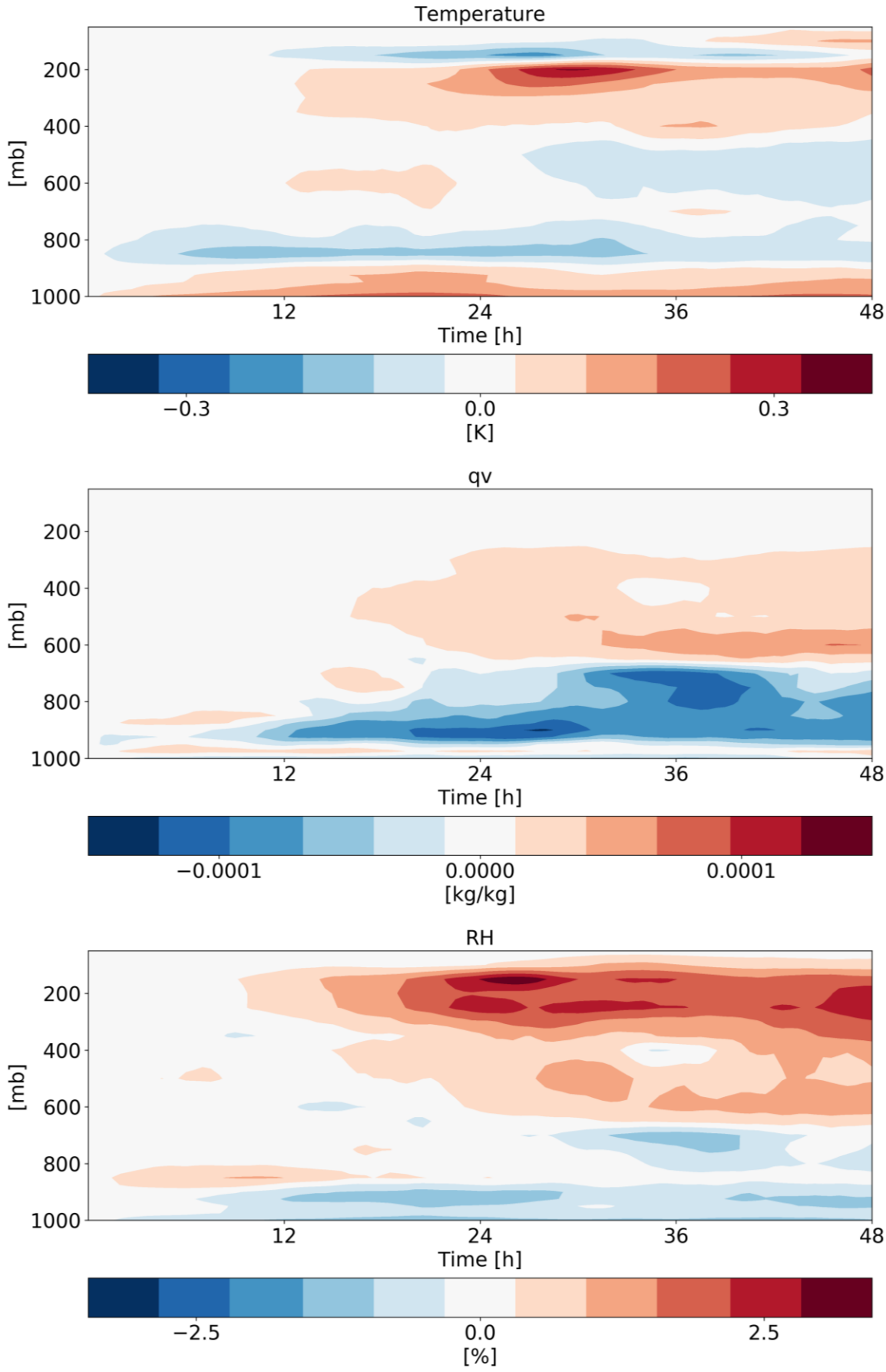

531

532 **Figure 18. Time-height diagrams of the differences in the domain mean temperature, specific humidity (qv)**

and relative humidity (RH) vertical profiles between polluted (CDNC = 200 cm^{-3}) and clean (CDNC = 20 cm^{-3}) simulations for the deep-cloud dominated case (16-18/08/2016).

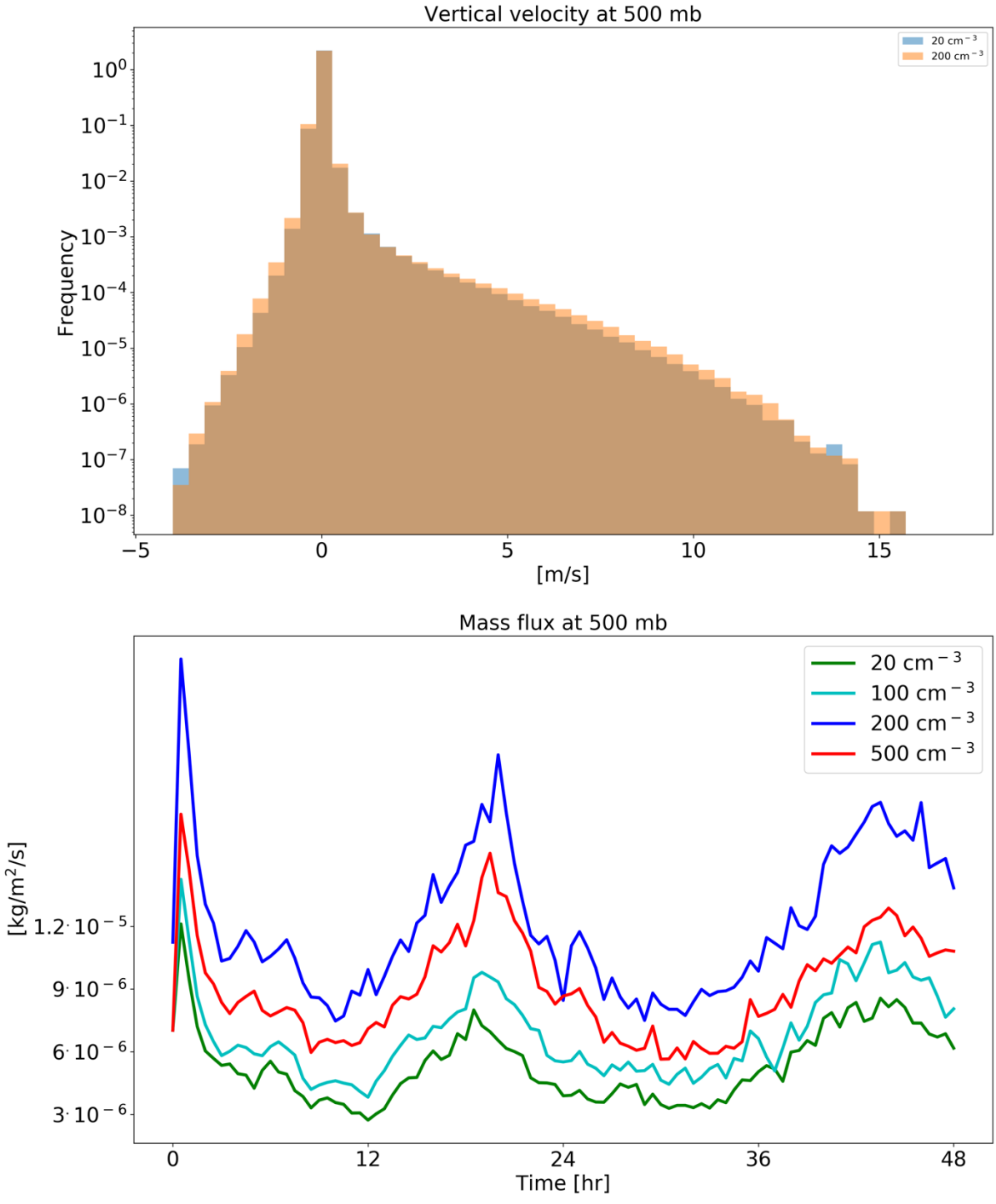

Figure 19. histograms of ICON simulated vertical velocity at the level of 500 mb for a clean (CDNC = 20 cm^{-3}) and polluted (CDNC = 200 cm^{-3}) simulations (upper), and the time evolution of the net upwards water (liquid and ice) mass flux (lower) for the different CDNC simulations for the deep-cloud dominated case (16-

18/08/2016). The 500 mb level is chosen as it represents the transition between the warm part to the cold part of the clouds. In the histogram only two simulations are presented for clarity.

Summary and conclusions

Two different case studies of tropical cloud systems over the Atlantic Ocean were simulated using the ICON numerical model in a cloud resolving configuration with 1.2 km resolution and a relatively large domain (~22° x 11°). The cases represent dates from the NARVAL 2 field campaign that took place during August 2016 and have different dominant cloud types and different dominating terms in their energy budget. The first case (10-12/8/2016) is shallow-cloud dominated and hence dominated by radiative cooling, while the second case (16-18/8/2016) is dominated by deep convective clouds and hence dominated by precipitation warming. The main objective of this study is to analyse the response of the atmospheric energy budget to changes in cloud droplet number concentration (CDNC), which serve as a proxy for (or idealized representation of) changes in aerosol concentration. This enables better understanding of the processes acting in global-scale studies trying to constrain aerosol effect on precipitation changes using the energy budget perspective (O'Gorman et al., 2012; Muller and O'Gorman, 2011; Hodnebrog et al., 2016; Samset et al., 2016; Myhre et al., 2017; Liu et al., 2018; Richardson et al., 2018; Dagan et al., 2019a). Our results demonstrate that regional atmospheric energy budgets can be significantly perturbed by changes in CDNC and that the magnitude of the effect is cloud regime dependent (even for a given geographical region and given time of the year as the two cases are separated by less than a week).

Figure 20 summarizes the energy and radiation response of the two simulated cases to CDNC perturbations. It shows that the atmosphere in the deep-cloud dominated case experiences a very strong atmospheric warming due to an increase in CDNC (10.0 W/m^2). Most of this warming is caused by a reduction in the outgoing LW radiation at the TOA. The SW radiative fluxes (both at the TOA and surface) is also significantly modified but their net effect on the atmospheric column energy budget is small. The net TOA radiative fluxes change in this case is -1.9 W/m^2. Beside the atmospheric radiative warming, changes in precipitation (~-0.3 W/m^2), and in sensible heat flux (Q_{SH}, -1.4 W/m^2) also contribute to the total trend as a response of increase in CDNC. We note that since 1 mm/hr of rain is equivalent to 628 W/m^2, even negligible changes in precipitation of less than 0.5 mm over 48 hr (as seen in our simulations) can still appear as significant changes in the atmospheric energy budget and contribute a few W/m^2.

The response of the radiative fluxes can be explained by the changes in the mean cloud and thermodynamic properties in the domain. The mean cloud fraction (CF) increases with the increase in CDNC (Fig. 16) while the vertical structure of it indicates a reduction in the low cloud fraction (below 800 mb) and an increase in the mid and upper troposphere CF (Fig. 17). The water content (both liquid and ice) also increase with the increase in CDNC (Figs. 16 and 17) with increasing amount with height. These changes in the mean cloud properties drive both the reduction in SW fluxes at TOA and surface and LW flux at TOA as the clouds become more opaque (Koren et al., 2010; Storelvmo et al., 2011) and cover a larger fraction of the sky. In addition to cloud responses, the domain-mean thermodynamic conditions change as well (Fig. 18). Specifically, the humidity content at the mid and upper troposphere increases with higher CDNC, (due to increase mass flux to the upper troposphere) which further decreases the outgoing LW flux at the TOA. However, the vast majority of the LW effect emerges from the changes in clouds.

Both the increase in water vapor and ice content in the upper troposphere are driven by an increase in water mass flux with increasing CDNC to these levels (Fig. 19, (Koren et al., 2005; Rosenfeld et al., 2008; Altaratz et al., 2014; Chen et al., 2017)), which is caused mostly by the increase in the water mixing ratio in the mid-troposphere rather than by increase in vertical velocity (Fig. 19) or in cloud fraction (Fig. 17). The ice content in the upper troposphere is also increased due to reduction in the ice falling speed (Grabowski and Morrison, 2016), while the increased relative humidity at these levels, further increases the ice particle lifetime due to slower evaporation. However, the increase in water mass flux to the upper layers is not accompanied with an increase in precipitation as predicted by the classical "invigoration" paradigm (Altaratz et al., 2014; Rosenfeld et al., 2008), which suggest that some compensating mechanisms are operating (Stevens and Feingold, 2009).

In the shallow-cloud dominated case (which also contains a significant amount of deep convection), the response of Q_R is weaker but still substantial (a total decrease in the atmospheric radiative cooling of 1.6 W/m^2 - Fig. 20). The weaker total response under the shallow-cloud dominated conditions is due to the smaller role of the ice part in this case. Here again, the changes in Q_{SH} decrease about -1.4 W/m^2 of this atmospheric warming. As in the deep-cloud dominated case, most of the atmospheric radiative warming is caused by reduction in the outgoing LW flux, while the surface and TOA SW fluxes changes are non-negligible but cancel each other out (in terms of the atmospheric energy budget – reflecting small SW atmospheric absorption changes). However, a significant TOA net (SW+LW) radiative flux change of ~-5.2 W/m^2 remains. In this

case, the cloud-mean effect on radiation is more complicated. While CF decreases with increasing CDNC, the mean water path (both LWP and IWP) increases (Fig. 8). As in the deep-cloud dominated case, the increase in the water content occurs mostly at the mid and upper troposphere, while the decrease in CF occurs mostly in the lower troposphere (Fig. 9). In terms of the SW fluxes, the effect of the decrease in low CF (decrease SW reflections) and the increase in water mass (increase SW reflections) would partially compensate, while the Twomey effect (Twomey, 1977) adds to the increase SW reflections. In this case, the net effect is more SW reflected back to space at TOA and a net negative flux change (including also the LW).

There exists a large spread in estimates of aerosol effects on clouds for different cloud types and different environmental conditions. In this study, as we use a relatively large domain (22^o x 11^o) and two different dates (each for two days), we sample many different local environmental conditions and cloud types. Such more realistic setups (although with lower spatial resolution) could provide more reliable estimates of aerosol effects on heterogeneous cloud systems than just one-cloud-type, small domain simulations (as was done in many previous studies, e.g (Dagan et al., 2017; Seifert et al., 2015; Ovchinnikov et al., 2014)). However, the conclusions demonstrated here are based on two specific cases. In order to examine the validity of our main conclusions over a wider range of initial conditions, we have conducted a large ensemble of simulations starting from realistic initial conditions (although with a smaller domain) in a companion paper (Dagan and Stier, 2019). These simulations demonstrate that the main conclusions presented in this paper are robust and hold also for a wide range of initial conditions representative for this area. In addition, the realistic setup with the continuously changing boundary conditions and systems that pass through the domain, which are used here, prevent conclusions that might be valid only in cyclic double periodic large eddy simulations, as the background meteorological conditions change more realistically (Dagan et al., 2018b). Another uncertainty in the assessment of the aerosol response are the large differences between different models and microphysical schemes (White et al., 2017; Fan et al., 2016; Khain et al., 2015; Heikenfeld et al., 2019). In this study, as we use only one model, we do not address this uncertainty. In future work we intend to examine the response in multiple models. In addition, more detailed observational constraints on the models are needed. Furthermore, we do not include the temporal evolution of the aerosol concentration. Feedbacks between the aerosol concentration and clouds processes (such as wet scavenging), as well as the direct effects of aerosol on radiation would add another layer of complexity that should be accounted for in future work.

Generally, the global mean aerosol radiative forcing is estimated to be negative (Boucher et al., 2013; Bellouin et al., 2019). However, these global aerosol forcing estimates have so far not included the radiative forcing associated with potential effects of aerosols on deep convection – and these effects are not represented in most current climate models due to limitations in convection parameterisations, with only a few exceptions (Kipling et al., 2017; Labbouz et al., 2018). Here we demonstrate the existence of non-negligible aerosol radiative effects (of -5.2 and -1.9 W/m^2 for the shallow and deep cloud dominated cases, respectively) in tropical cloud systems, that contained both deep and shallow convective clouds, with significant SW and LW contributions. From the (limited) two cases simulated here, it appears that (in agreement with previous studies) the aerosol effect may be regime dependent and that even within a given cloud regime the effect may vary with the meteorological conditions.

Finally, we hypothesise that the aerosol impact shown on the atmospheric energy balance, with increasing divergence of dry static energy from deep convective regions concomitantly with increased convergence in shallow clouds regions, can have effects on the large-scale circulation. This should be investigated in future work.

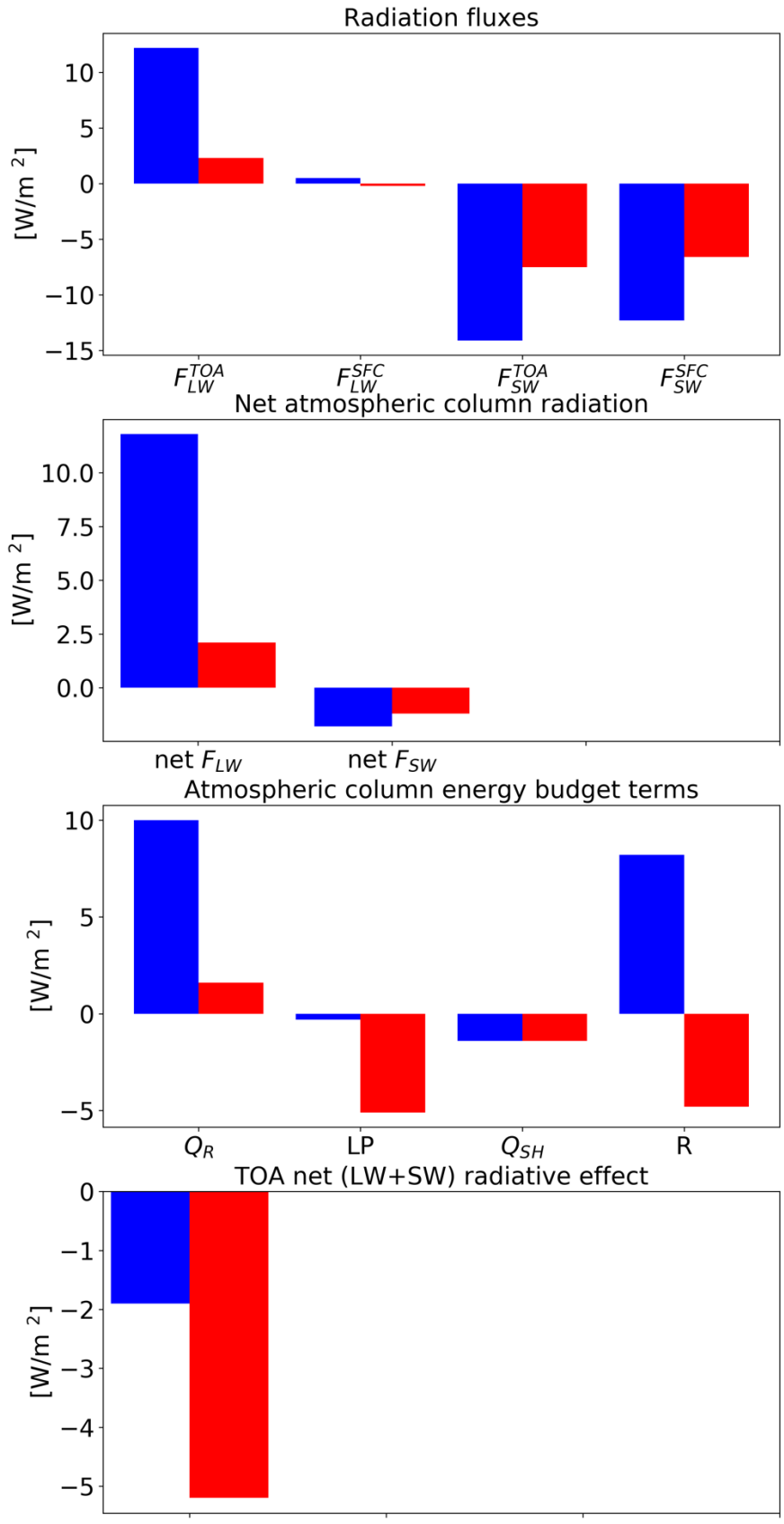

Figure 20. Summary of the radiation and energy response to CDNC perturbation in the two different cases. Blue represent the deep-cloud dominated case while red the shallow-cloud dominated case.

Author contributions. G. D. carried out the simulations and analyses presented. G.C., D.K. and A.S. assisted with the simulations. M.C. assisted with the radiative transfer calculations and comparison with observations. P. S. and A.S. assisted with the design and interpretation of the analyses. G. D. prepared the manuscript with contributions from all co-authors.

Acknowledgements:

This research was supported by the European Research Council (ERC) project constRaining the EffeCts of Aerosols on Precipitation (RECAP) under the European Union's Horizon 2020 research and innovation programme with grant agreement No 724602. The simulations were performed using the ARCHER UK National Supercomputing Service. ECMWF is acknowledged for providing Era-interim data set (https://apps.ecmwf.int/datasets/). We acknowledge MPI, DWD and DKRZ for the NARVAL simulations. The data presented in the paper can be find in: https://zenodo.org/record/3611366#.Xi7rHC-cbUI DOI:10.5281/zenodo.3611366

References

Albrecht, B. A.: Aerosols, cloud microphysics, and fractional cloudiness, Science (New York, NY), 245, 1227, DOI: 10.1126/science.245.4923.1227, 1989.

Albrecht, B. A.: Effects of precipitation on the thermodynamic structure of the trade wind boundary layer, Journal of Geophysical Research: Atmospheres (1984–2012), 98, 7327-7337, https://doi.org/10.1029/93JD00027, 1993.

Altaratz, O., Koren, I., Remer, L., and Hirsch, E.: Review: Cloud invigoration by aerosols—Coupling between microphysics and dynamics, Atmospheric Research, 140, 38-60, https://doi.org/10.1016/j.atmosres.2014.01.009, 2014.

Aminou, D.: MSG's SEVIRI instrument, ESA Bulletin (0376-4265), 15-17, 2002.

Andreae, M. O., Rosenfeld, D., Artaxo, P., Costa, A. A., Frank, G. P., Longo, K. M., and Silva-Dias, M. A. F.: Smoking rain clouds over the Amazon, Science, 303, 1337-1342, 10.1126/science.1092779, 2004.

Andreae, M. O.: Correlation between cloud condensation nuclei concentration and aerosol optical thickness in remote and polluted regions, Atmospheric Chemistry and Physics, 9.2, 543-556, 2009.

Arakawa, A., and Schubert, W. H.: Interaction of a cumulus cloud ensemble with the large-scale environment, Part I, Journal of the Atmospheric Sciences, 31, 674-701, 1974.

Bellouin, N., Quaas, J., Gryspeerdt, E., Kinne, S., Stier, P., Watson-Parris, D., Boucher, O., Carslaw, K., Christensen, M., and Daniau, A.-L.: Bounding aerosol radiative forcing of climate change, Reviews of Geophysics, http://hdl.handle.net/21.11116/0000-0003-9D8D-E, 2019.

Boucher, O., Randall, D., Artaxo, P., Bretherton, C., Feingold, G., Forster, P., Kerminen, V., Kondo, Y., Liao, H., and Lohmann, U.: Clouds and aerosols, Climate Change, 571-657, 2013.

Chen, Q., Koren, I., Altaratz, O., Heiblum, R. H., Dagan, G., and Pinto, L.: How do changes in warm-phase microphysics affect deep convective clouds?, Atmospheric Chemistry and Physics, 17, 9585-9598, https://doi.org/10.5194/acp-17-9585-2017, 2017.

694 Christensen, M. W., Chen, Y. C., and Stephens, G. L.: Aerosol indirect effect dictated by liquid clouds,
695 Journal of Geophysical Research: Atmospheres, 121, https://doi.org/10.1002/2016JD025245, 2016.
696 Clough, S., Shephard, M., Mlawer, E., Delamere, J., Iacono, M., Cady-Pereira, K., Boukabara, S., and
697 Brown, P.: Atmospheric radiative transfer modeling: a summary of the AER codes, Journal of
698 Quantitative Spectroscopy and Radiative Transfer, 91, 233-244,
699 https://doi.org/10.1016/j.jqsrt.2004.05.058, 2005.
700 Costantino, L., and Bréon, F.-M.: Aerosol indirect effect on warm clouds over South-East Atlantic,
701 from co-located MODIS and CALIPSO observations, Atmospheric Chemistry and Physics, 13, 69-88,
702 2013.
703 Dagan, G., Koren, I., and Altaratz, O.: Aerosol effects on the timing of warm rain processes,
704 Geophysical Research Letters, 42, 4590-4598, 10.1002/2015GL063839, 2015a.
705 Dagan, G., Koren, I., and Altaratz, O.: Competition between core and periphery-based processes in
706 warm convective clouds–from invigoration to suppression, Atmospheric Chemistry and Physics, 15,
707 2749-2760, https://doi.org/10.5194/acp-15-2749-2015, 2015b.
708 Dagan, G., and Chemke, R.: The effect of subtropical aerosol loading on equatorial precipitation,
709 Geophysical Research Letters, 43, https://doi.org/10.1002/2016GL071206, 2016.
710 Dagan, G., Koren, I., Altaratz, O., and Heiblum, R. H.: Aerosol effect on the evolution of the
711 thermodynamic properties of warm convective cloud fields, Scientific Reports, 6, 38769, DOI:
712 10.1038/srep38769, 2016.
713 Dagan, G., Koren, I., Altaratz, O., and Heiblum, R. H.: Time-dependent, non-monotonic response of
714 warm convective cloud fields to changes in aerosol loading, Atmos. Chem. Phys., 17, 7435-7444,
715 10.5194/acp-17-7435-2017, 2017.
716 Dagan, G., Koren, I., and Altaratz, O.: Quantifying the effect of aerosol on vertical velocity and
717 effective terminal velocity in warm convective clouds, Atmospheric Chemistry and Physics, 18, 6761-
718 6769, https://doi.org/10.5194/acp-18-6761-2018, 2018a.
719 Dagan, G., Koren, I., Altaratz, O., and Lehahn, Y.: Shallow convective cloud field lifetime as a key
720 factor for evaluating aerosol effects, iScience, 10, 192-202,
721 https://doi.org/10.1016/j.isci.2018.11.032, 2018b.
722 Dagan, G., Koren, I., Kostinski, A., and Altaratz, O.: Organization and oscillations in simulated shallow
723 convective clouds, Journal of Advances in Modeling Earth Systems,
724 https://doi.org/10.1029/2018MS001416, 2018c.
725 Dagan, G., Stier, P., and Watson-Parris, D.: Contrasting response of precipitation to aerosol
726 perturbation in the tropics and extra-tropics explained by energy budget considerations, Geophysical
727 Research Letters, https://doi.org/10.1029/2019GL083479, 2019a.
728 Dagan, G., Stier, P., and Watson-Parris, D.: Analysis of the atmospheric water budget for elucidating
729 the spatial scale of precipitation changes under climate change, Geophysical Research Letters,
730 https://doi.org/10.1029/2019GL084173, 2019b
731 Dagan, G. and Stier, P.: Ensemble daily simulations for elucidating cloud–aerosol interactions under a
732 large spread of realistic environmental conditions, Atmos. Chem. Phys. Discuss.,
733 https://doi.org/10.5194/acp-2019-949, in review, 2019.
734 Dee, D., Uppala, S., Simmons, A., Berrisford, P., Poli, P., Kobayashi, S., Andrae, U., Balmaseda, M.,
735 Balsamo, G., and Bauer, P.: The ERA-Interim reanalysis: Configuration and performance of the data
736 assimilation system, Quarterly Journal of the royal meteorological society, 137, 553-597,
737 https://doi.org/10.1002/qj.828, 2011.

738 Dey, S., Di Girolamo, L., Zhao, G., Jones, A. L., and McFarquhar, G. M.: Satellite-observed
739 relationships between aerosol and trade-wind cumulus cloud properties over the Indian Ocean,
740 Geophysical Research Letters, 38, https://doi.org/10.1029/2010GL045588, 2011.
741 Emanuel, K. A., Neelin, J. D., and Bretherton, C. S.: On large-scale circulations in convecting
742 atmospheres, Quarterly Journal of the Royal Meteorological Society, 120, 1111-1143, 1994.
743 Fan, J., Zhang, R., Li, G., and Tao, W.-K.: Effects of aerosols and relative humidity on cumulus clouds,
744 Journal of Geophysical Research-Atmospheres, 112, 10.1029/2006jd008136, 2007.
745 Fan, J., Yuan, T., Comstock, J. M., Ghan, S., Khain, A., Leung, L. R., Li, Z., Martins, V. J., and
746 Ovchinnikov, M.: Dominant role by vertical wind shear in regulating aerosol effects on deep
747 convective clouds, Journal of Geophysical Research-Atmospheres, 114, 10.1029/2009jd012352,
748 2009.
749 Fan, J., Comstock, J. M., and Ovchinnikov, M.: The cloud condensation nuclei and ice nuclei effects
750 on tropical anvil characteristics and water vapor of the tropical tropopause layer, Environmental
751 Research Letters, 5, 10.1088/1748-9326/5/4/044005, 2010.
752 Fan, J., Leung, L. R., Rosenfeld, D., Chen, Q., Li, Z., Zhang, J., and Yan, H.: Microphysical effects
753 determine macrophysical response for aerosol impacts on deep convective clouds, Proceedings of
754 the National Academy of Sciences, 110, E4581-E4590, https://doi.org/10.1073/pnas.1316830110,
755 2013.
756 Fan, J., Wang, Y., Rosenfeld, D., and Liu, X.: Review of aerosol–cloud interactions: Mechanisms,
757 significance, and challenges, Journal of the Atmospheric Sciences, 73, 4221-4252,
758 https://doi.org/10.1175/JAS-D-16-0037.1, 2016.
759 Ghan, S. J., Abdul-Razzak, H., Nenes, A., Ming, Y., Liu, X., Ovchinnikov, M., Shipway, B., Meskhidze,
760 N., Xu, J., and Shi, X.: Droplet nucleation: Physically-based parameterizations and comparative
761 evaluation, Journal of Advances in Modeling Earth Systems, 3,
762 https://doi.org/10.1029/2011MS000074, 2011.
763 Glassmeier, F., and Lohmann, U.: Constraining precipitation susceptibility of warm-, ice-, and mixed-
764 phase clouds with microphysical equations, Journal of the Atmospheric Sciences, 73, 5003-5023,
765 https://doi.org/10.1175/JAS-D-16-0008.1, 2016.
766 Goren, T., and Rosenfeld, D.: Decomposing aerosol cloud radiative effects into cloud cover, liquid
767 water path and Twomey components in marine stratocumulus, Atmospheric research, 138, 378-393,
768 https://doi.org/10.1016/j.atmosres.2013.12.008, 2014.
769 Grabowski, W. W., and Morrison, H.: Untangling microphysical impacts on deep convection applying
770 a novel modeling methodology. Part II: Double-moment microphysics, Journal of the Atmospheric
771 Sciences, 73, 3749-3770, https://doi.org/10.1175/JAS-D-15-0367.1, 2016.
772 Gryspeerdt, E., and Stier, P.: Regime-based analysis of aerosol-cloud interactions, Geophysical
773 Research Letters, 39, https://doi.org/10.1029/2012GL053221, 2012.
774 Gryspeerdt, E., Stier, P., White, B., and Kipling, Z.: Wet scavenging limits the detection of aerosol
775 effects on precipitation, Atmospheric Chemistry and Physics, 15, 7557-7570,
776 https://doi.org/10.5194/acp-15-7557-2015, 2015.
777 Gryspeerdt, E., Sourdeval, O., Quaas, J., Delanoë, J., Krämer, M., and Kühne, P.: Ice crystal number
778 concentration estimates from lidar–radar satellite remote sensing–Part 2: Controls on the ice crystal
779 number concentration, Atmospheric Chemistry and Physics, 18, 14351-14370,
780 https://doi.org/10.5194/acp-18-14351-2018, 2018b.

781 Gryspeerdt, E., Goren, T., Sourdeval, O., Quaas, J., Mülmenstädt, J., Dipu, S., Unglaub, C., Gettelman,
782 A., and Christensen, M.: Constraining the aerosol influence on cloud liquid water path, Atmospheric
783 Chemistry and Physics, 19, 5331-5347, https://doi.org/10.5194/acp-19-5331-2019, 2019.
784 Heikenfeld, M., White, B., Labbouz, L., and Stier, P.: Aerosol effects on deep convection: the
785 propagation of aerosol perturbations through convective cloud microphysics, Atmospheric
786 Chemistry and Physics, 19, 2601-2627, https://doi.org/10.5194/acp-19-2601-2019, 2019.
787 Henderson, D. S., L'Ecuyer, T., Stephens, G., Partain, P., and Sekiguchi, M.: A Multisensor Perspective
788 on the Radiative Im- pacts of Clouds and Aerosols, J. Appl. Meteorol. Clim., 52, 853– 871,
789 https://doi.org/10.1175/JAMC-D-12-025.1, 2013.
790 Hodnebrog, O., Myhre, G., Forster, P. M., Sillmann, J., and Samset, B. H.: Local biomass burning is a
791 dominant cause of the observed precipitation reduction in southern Africa, Nat Commun, 7,
792 10.1038/ncomms11236, 2016.
793 Hoose, C., and Möhler, O.: Heterogeneous ice nucleation on atmospheric aerosols: a review of
794 results from laboratory experiments, Atmo-30 spheric Chemistry and Physics, 12, 9817–9854. 2012.
795 Iacono, M. J., Delamere, J. S., Mlawer, E. J., Shephard, M. W., Clough, S. A., and Collins, W. D.:
796 Radiative forcing by long-lived greenhouse gases: Calculations with the AER radiative transfer
797 models, Journal of Geophysical Research: Atmospheres, 113,
798 https://doi.org/10.1029/2008JD009944, 2008.
799 Jakob, C., Singh, M., and Jungandreas, L.: Radiative Convective Equilibrium and Organized
800 Convection: An Observational Perspective, Journal of Geophysical Research: Atmospheres, 124,
801 5418-5430, 2019.
802 Jeon, Y.-L., Moon, S., Lee, H., Baik, J.-J., and Lkhamjav, J.: Non-Monotonic Dependencies of Cloud
803 Microphysics and Precipitation on Aerosol Loading in Deep Convective Clouds: A Case Study Using
804 the WRF Model with Bin Microphysics, Atmosphere, 9, 434, https://doi.org/10.3390/atmos9110434,
805 2018.
806 Jiang, H., Xue, H., Teller, A., Feingold, G., and Levin, Z.: Aerosol effects on the lifetime of shallow
807 cumulus, Geophysical Research Letters, 33, 10.1029/2006gl026024, 2006.
808 Jiang, J. H., Su, H., Huang, L., Wang, Y., Massie, S., Zhao, B., Omar, A., and Wang, Z.: Contrasting
809 effects on deep convective clouds by different types of aerosols, Nature communications, 9, 3874,
810 2018.
811 Kalina, E. A., Friedrich, K., Morrison, H., and Bryan, G. H.: Aerosol effects on idealized supercell
812 thunderstorms in different environments, Journal of the Atmospheric Sciences, 71, 4558-4580,
813 https://doi.org/10.1175/JAS-D-14-0037.1, 2014.
814 Kaufman, Y. J., Koren, I., Remer, L. A., Rosenfeld, D., and Rudich, Y.: The effect of smoke, dust, and
815 pollution aerosol on shallow cloud development over the Atlantic Ocean, Proceedings of the
816 National Academy of Sciences of the United States of America, 102, 11207-11212,
817 10.1073/pnas.0505191102, 2005.
818 Khain, A., Rosenfeld, D., and Pokrovsky, A.: Aerosol impact on the dynamics and microphysics of
819 deep convective clouds, Quarterly Journal of the Royal Meteorological Society, 131, 2639-2663,
820 10.1256/qj.04.62, 2005.
821 Khain, A., Beheng, K., Heymsfield, A., Korolev, A., Krichak, S., Levin, Z., Pinsky, M., Phillips, V.,
822 Prabhakaran, T., and Teller, A.: Representation of microphysical processes in cloud-resolving models:
823 spectral (bin) microphysics vs. bulk parameterization, Reviews of Geophysics,
824 https://doi.org/10.1002/2014RG000468, 2015.

825 Khain, A. P., BenMoshe, N., and Pokrovsky, A.: Factors determining the impact of aerosols on surface
826 precipitation from clouds: An attempt at classification, Journal of the Atmospheric Sciences, 65,
827 1721-1748, 10.1175/2007jas2515.1, 2008.
828 Khain, A. P.: Notes on state-of-the-art investigations of aerosol effects on precipitation: a critical
829 review, Environmental Research Letters, 4, 015004 (015020 pp.)-015004 (015020 pp.),
830 10.1088/1748-9326/4/1/015004, 2009.
831 Kipling, Z., Stier, P., Labbouz, L., and Wagner, T.: Dynamic subgrid heterogeneity of convective cloud
832 in a global model: description and evaluation of the Convective Cloud Field Model (CCFM) in
833 ECHAM6–HAM2, Atmospheric Chemistry and Physics, 17, 327-342, https://doi.org/10.5194/acp-17-
834 327-2017, 2017.
835 Klepp, C., Ament, F., Bakan, S., Hirsch, L., and Stevens, B.: The NARVAL Campaign Report, 2014.
836 Klocke, D., Brueck, M., Hohenegger, C., and Stevens, B.: Rediscovery of the doldrums in storm-
837 resolving simulations over the tropical Atlantic, Nature Geoscience, 10, 891, 2017.
838 Koren, I., Kaufman, Y. J., Rosenfeld, D., Remer, L. A., and Rudich, Y.: Aerosol invigoration and
839 restructuring of Atlantic convective clouds, Geophysical Research Letters, 32,
840 10.1029/2005gl023187, 2005.
841 Koren, I., Remer, L. A., Altaratz, O., Martins, J. V., and Davidi, A.: Aerosol-induced changes of
842 convective cloud anvils produce strong climate warming, Atmospheric Chemistry and Physics, 10,
843 5001-5010, 10.5194/acp-10-5001-2010, 2010.
844 Koren, I., Dagan, G., and Altaratz, O.: From aerosol-limited to invigoration of warm convective
845 clouds, science, 344, 1143-1146, DOI: 10.1126/science.1252595, 2014.
846 Koren, I., Altaratz, O., and Dagan, G.: Aerosol effect on the mobility of cloud droplets, Environmental
847 Research Letters, 10, 104011, doi:10.1088/1748-9326/10/10/104011, 2015.
848 Labbouz, L., Kipling, Z., Stier, P., and Protat, A.: How Well Can We Represent the Spectrum of
849 Convective Clouds in a Climate Model? Comparisons between Internal Parameterization Variables
850 and Radar Observations, Journal of the Atmospheric Sciences, 75, 1509-1524,
851 https://doi.org/10.1175/JAS-D-17-0191.1, 2018.
852 Lebo, Z. J., and Morrison, H.: Dynamical effects of aerosol perturbations on simulated idealized
853 squall lines, Monthly Weather Review, 142, 991-1009, 2014.
854 Lee, S.-S., Feingold, G., and Chuang, P. Y.: Effect of aerosol on cloud–environment interactions in
855 trade cumulus, Journal of the Atmospheric Sciences, 69, 3607-3632, 2012.
856 Lee, S. S., Donner, L. J., and Phillips, V. T. J.: Sensitivity of aerosol and cloud effects on radiation to
857 cloud types: comparison between deep convective clouds and warm stratiform clouds over one-day
858 period, Atmospheric Chemistry and Physics, 9, 2555-2575, 2009.
859 Levin, Z., and Cotton, W. R.: Aerosol pollution impact on precipitation: A scientific review, Springer,
860 2009.
861 Liu, H., Guo, J., Koren, I., Altaratz, O., Dagan, G., Wang, Y., Jiang, J. H., Zhai, P., and Yung, Y. L.: Non-
862 Monotonic Aerosol Effect on Precipitation in Convective Clouds over Tropical Oceans, Scientific
863 Reports, 9, 7809, 2019.
864 Liu, L., Shawki, D., Voulgarakis, A., Kasoar, M., Samset, B., Myhre, G., Forster, P., Hodnebrog, Ø.,
865 Sillmann, J., and Aalbergsjø, S.: A PDRMIP Multimodel Study on the impacts of regional aerosol
866 forcings on global and regional precipitation, Journal of Climate, 31, 4429-4447, 2018.
867 Lohmann, U., and Hoose, C.: Sensitivity studies of different aerosol indirect effects in mixed-phase
868 clouds, Atmospheric Chemistry and Physics, 9, 8917-8934, 2009.

Manabe, S., and Strickler, R. F.: Thermal equilibrium of the atmosphere with a convective adjustment, Journal of the Atmospheric Sciences, 21, 361-385, 1964

Mlawer, E. J., Taubman, S. J., Brown, P. D., Iacono, M. J., and Clough, S. A.: Radiative transfer for inhomogeneous atmospheres: RRTM, a validated correlated-k model for the longwave, Journal of Geophysical Research: Atmospheres, 102, 16663-16682, 1997.

Muller, C., and O'Gorman, P.: An energetic perspective on the regional response of precipitation to climate change, Nature Climate Change, 1, 266, 2011.

Mülmenstädt, J., and Feingold, G.: The Radiative Forcing of Aerosol–Cloud Interactions in Liquid Clouds: Wrestling and Embracing Uncertainty, Current Climate Change Reports, 4, 23-40, https://doi.org/10.1007/s40641-018-0089-y, 2018.

Myhre, G., Forster, P., Samset, B., Hodnebrog, Ø., Sillmann, J., Aalbergsjø, S., Andrews, T., Boucher, O., Faluvegi, G., and Fläschner, D.: PDRMIP: a precipitation driver and response model intercomparison project—protocol and preliminary results, Bulletin of the American Meteorological Society, 98, 1185-1198, 2017.

O'Gorman, P. A., Allan, R. P., Byrne, M. P., and Previdi, M.: Energetic Constraints on Precipitation Under Climate Change, Surveys in Geophysics, 33, 585-608, https://doi.org/10.1007/s10712-011-9159-6, 2012.

Ovchinnikov, M., Ackerman, A. S., Avramov, A., Cheng, A., Fan, J., Fridlind, A. M., Ghan, S., Harrington, J., Hoose, C., and Korolev, A.: Intercomparison of large-eddy simulations of Arctic mixed-phase clouds: Importance of ice size distribution assumptions, Journal of Advances in Modeling Earth Systems, 6, 223-248, https://doi.org/10.1002/2013MS000282, 2014.

Richardson, T., Forster, P., Andrews, T., Boucher, O., Faluvegi, G., Fläschner, D., Hodnebrog, Ø., Kasoar, M., Kirkevåg, A., and Lamarque, J.-F.: Drivers of precipitation change: An energetic understanding, Journal of Climate, 31, 9641-9657, https://doi.org/10.1175/JCLI-D-17-0240.1, 2018.

Rosenfeld, D.: Suppression of rain and snow by urban and industrial air pollution, Science, 287, 1793-1796, 10.1126/science.287.5459.1793, 2000.

Rosenfeld, D., Lohmann, U., Raga, G. B., O'Dowd, C. D., Kulmala, M., Fuzzi, S., Reissell, A., and Andreae, M. O.: Flood or drought: How do aerosols affect precipitation?, Science, 321, 1309-1313, 10.1126/science.1160606, 2008.

Rosenfeld, D., Wood, R., Donner, L. J., and Sherwood, S. C.: Aerosol cloud-mediated radiative forcing: highly uncertain and opposite effects from shallow and deep clouds, in: Climate Science for Serving Society, Springer, 105-149, https://doi.org/10.1007/978-94-007-6692-1_5, 2013.

Rosenfeld, D., Zhu, Y., Wang, M., Zheng, Y., Goren, T., and Yu, S.: Aerosol-driven droplet concentrations dominate coverage and water of oceanic low-level clouds, Science, 363, eaav0566, DOI: 10.1126/science.aav0566, 2019.

Rothenberg, D., Avramov, A., and Wang, C.: On the representation of aerosol activation and its influence on model-derived estimates of the aerosol indirect effect, Atmos. Chem. Phys, 18, 7961-7983, https://doi.org/10.5194/acp-18-7961-2018, 2018.

Samset, B., Myhre, G., Forster, P., Hodnebrog, Ø., Andrews, T., Faluvegi, G., Flaeschner, D., Kasoar, M., Kharin, V., and Kirkevåg, A.: Fast and slow precipitation responses to individual climate forcers: A PDRMIP multimodel study, Geophysical Research Letters, 43, 2782-2791, https://doi.org/10.1002/2016GL068064, 2016.

Savane, O. S., Vant-Hull, B., Mahani, S., and Khanbilvardi, R.: Effects of Aerosol on Cloud Liquid Water Path: Statistical Method a Potential Source for Divergence in Past Observation Based Correlative Studies, Atmosphere, 6, 273-298, https://doi.org/10.3390/atmos6030273, 2015.

914 Seifert, A., and Beheng, K.: A two-moment cloud microphysics parameterization for mixed-phase
915 clouds. Part 2: Maritime vs. continental deep convective storms, Meteorology and Atmospheric
916 Physics, 92, 67-82, https://doi.org/10.1007/s00703-005-0113-3, 2006a.
917 Seifert, A., and Beheng, K. D.: A two-moment cloud microphysics parameterization for mixed-phase
918 clouds. Part 1: Model description, Meteorology and atmospheric physics, 92, 45-66,
919 https://doi.org/10.1007/s00703-005-0112-4, 2006b.
920 Seifert, A., and Heus, T.: Large-eddy simulation of organized precipitating trade wind cumulus
921 clouds, Atmos. Chem. Phys, 13, 5631-5645, doi:10.5194/acpd-13-1855-2013, 2013.
922 Seifert, A., Heus, T., Pincus, R., and Stevens, B.: Large-eddy simulation of the transient and near-
923 equilibrium behavior of precipitating shallow convection, Journal of Advances in Modeling Earth
924 Systems, https://doi.org/10.1002/2015MS000489, 2015.
925 Seigel, R. B.: Shallow Cumulus Mixing and Subcloud Layer Responses to Variations in Aerosol
926 Loading, Journal of the Atmospheric Sciences, https://doi.org/10.1175/JAS-D-13-0352.1, 2014.
927 Simpson, E., Connolly, P., and McFiggans, G.: An investigation into the performance of four cloud
928 droplet activation parameterisations, Geoscientific Model Development, 7, 1535-1542,
929 doi:10.5194/gmd-7-1535-2014, 2014.
930 Small, J. D., Chuang, P. Y., Feingold, G., and Jiang, H.: Can aerosol decrease cloud lifetime?,
931 Geophysical Research Letters, 36, https://doi.org/10.1029/2009GL038888, 2009.
932 Sourdeval, O., Gryspeerdt, E., Krämer, M., Goren, T., Delanoë, J., Afchine, A., Hemmer, F., and Quaas,
933 J.: Ice crystal number concentration estimates from lidar–radar satellite remote sensing–Part 1:
934 Method and evaluation, https://doi.org/10.5194/acp-18-14327-2018 2018.
935 Spill, G., Stier, P., Field, P. R., and Dagan, G.: Effects of aerosol in simulations of realistic shallow
936 cumulus cloud fields in a large domain, Atmospheric Chemistry and Physics,
937 https://doi.org/10.5194/acp-2019-432, 2019.
938 Stephens, G. L., Gabriel, P. M., and Partain, P. T.: Parameterization of atmospheric radiative transfer.
939 Part I: Validity of simple models, Journal of the atmospheric sciences, 58, 3391-3409,
940 https://doi.org/10.1175/1520-0469(2001)058%3C3391:POARTP%3E2.0.CO;2, 2001.
941 Stevens, B., and Feingold, G.: Untangling aerosol effects on clouds and precipitation in a buffered
942 system, Nature, 461, 607-613, 10.1038/nature08281, 2009.
943 Stevens, B., Farrell, D., Hirsch, L., Jansen, F., Nuijens, L., Serikov, I., Brügmann, B., Forde, M., Linne,
944 H., and Lonitz, K.: The Barbados Cloud Observatory: Anchoring investigations of clouds and
945 circulation on the edge of the ITCZ, Bulletin of the American Meteorological Society, 97, 787-801,
946 2016.
947 Stevens, B., Ament, F., Bony, S., Crewell, S., Ewald, F., Gross, S., Hansen, A., Hirsch, L., Jacob, M., and
948 Kölling, T.: A high-altitude long-range aircraft configured as a cloud observatory–the NARVAL
949 expeditions, Bulletin of the American Meteorological Society, https://doi.org/10.1175/BAMS-D-18-
950 0198.1, 2019.
951 Storelvmo, T., Hoose, C., and Eriksson, P.: Global modeling of mixed-phase clouds: The albedo and
952 lifetime effects of aerosols, Journal of Geophysical Research: Atmospheres, 116,
953 https://doi.org/10.1029/2010JD014724, 2011.
954 Tao, W.-K., Chen, J.-P., Li, Z., Wang, C., and Zhang, C.: Impact of aerosols on convective clouds and
955 precipitation, Reviews of Geophysics, 50, RG2001, https://doi.org/10.1029/2011RG000369, 2012.
956 Twomey, S.: The influence of pollution on the shortwave albedo of clouds, Journal of the
957 atmospheric sciences, 34, 1149-1152, 1977.

van den Heever, S. C., Stephens, G. L., and Wood, N. B.: Aerosol Indirect Effects on Tropical Convection Characteristics under Conditions of Radiative-Convective Equilibrium, Journal of the Atmospheric Sciences, 68, 699-718, 10.1175/2010jas3603.1, 2011.

Varble, A.: Erroneous attribution of deep convective invigoration to aerosol concentration, Journal of the Atmospheric Sciences, 75, 1351-1368, https://doi.org/10.1175/JAS-D-17-0217.1, 2018.

White, B., Gryspeerdt, E., Stier, P., Morrison, H., Thompson, G., and Kipling, Z.: Uncertainty from choice of microphysics scheme in convection-permitting models significantly exceeds aerosol effects, Atmospheric Chemistry and Physics, 7, https://doi.org/10.5194/acp-17-12145-2017, 2017.

Williams, E., Rosenfeld, D., Madden, N., Gerlach, J., Gears, N., Atkinson, L., Dunnemann, N., Frostrom, G., Antonio, M., and Biazon, B.: Contrasting convective regimes over the Amazon: Implications for cloud electrification, J. Geophys. Res, 107, https://doi.org/10.1029/2001JD000380, 2002.

Xue, H., and Feingold, G.: Large-eddy simulations of trade wind cumuli: Investigation of aerosol indirect effects, Journal of the atmospheric sciences, 63, 1605-1622, https://doi.org/10.1175/JAS3706.1, 2006.

Yuan, T., Remer, L. A., Pickering, K. E., and Yu, H.: Observational evidence of aerosol enhancement of lightning activity and convective invigoration, Geophysical Research Letters, 38, 10.1029/2010gl046052, 2011a.

Yuan, T., Remer, L. A., and Yu, H.: Microphysical, macrophysical and radiative signatures of volcanic aerosols in trade wind cumulus observed by the A-Train, Atmospheric Chemistry and Physics, 11, 7119-7132, 10.5194/acp-11-7119-2011, 2011b.

Zängl, G., Reinert, D., Rípodas, P., and Baldauf, M.: The ICON (ICOsahedral Non-hydrostatic) modelling framework of DWD and MPI-M: Description of the non-hydrostatic dynamical core, Quarterly Journal of the Royal Meteorological Society, 141, 563-579, https://doi.org/10.1002/qj.2378, 2015.